Mechanics of Materials 200 (2025) 105212

Contents lists available at ScienceDirect

Mechanics of Materials

journal homepage: www.elsevier.com/locate/mechmat

Research paper

Predicting the evolution of texture and grain size during deformation and recrystallization of polycrystals using field fluctuations viscoplastic self-consistent crystal plasticity

Iftekhar A. Riyad, Marko Knezevic *

Department of Mechanical Engineering, University of New Hampshire, Durham, NH, 03824, USA

ARTICLE INFO

Handling editor: G Subhash

Keywords:
Microstructures
Plastic deformation
Field fluctuations
Grain fragmentation
Recrystallization
FF-VPSC

ABSTRACT

This paper advances a recent formulation of a field fluctuations viscoplastic self-consistent (FF-VPSC) crystal plasticity model to predict not only the evolution of texture in polycrystalline metals undergoing deformation and recrystallization but also the evolution of grain size. The model considers stress and lattice rotation rate fluctuations inside grains to calculate intragranular misorientation spreads. The spreads are used for modeling of grain fragmentation during deformation and grain nucleation during recrystallization enabling the predictions of concomitant evolution of texture and grain size distributions. The evolutions of textures and grain size distributions are first simulated for commercially pure Cu undergoing severe plastic deformation (SPD) in high pressure torsion to agree well with corresponding experimental data. Next, the evolution of texture and grain size in an aluminum alloy (AA) 5182-O after simple tension and static recrystallization are predicted and compared with experiments. Finally, the predictions of texture and grain size distributions in a magnesium alloy WE43 undergoing a thermo-mechanical loading in the dynamic recrystallization regime are presented and compared with experiments. After validation, the model is coupled with the implicit finite element method (FEM) via a user-material subroutine (UMAT) in Abaqus to facilitate modeling of complex boundary conditions and geometries. The multilevel approach is referred to as FE-FF-VPSC in which every integration point embeds the FF-VPSC constitutive law, considering texture evolution and the directionality of deformation mechanisms operating at the single crystal level. FE-FF-VPSC is applied to simulate a sequence of rolling, recrystallization, and deep drawing of a circular cup of AA6022-T4. The simulated processing sequence demonstrates the versatility of the simulation framework developed in the present paper in not only predicting texture and grain size evolution and phenomena pertaining to behavior of materials but also geometrical shape changes important for the optimization of metal forming processes. To this end, the effects of initial texture and underlying anisotropy on the formation of earing profiles during deep drawing are simulated and discussed.

1. Introduction

Microstructural features such as crystallographic texture and grain size play important roles in the performance characteristics of polycrystalline metals (Hall, 1951; Kalidindi et al., 2009; Knezevic and Beyerlein, 2018; Kocks et al., 1998b; Petch, 1953). Refined grain structures result in a large content of grain boundary defects allowing greater resistance to dislocation motion and making the material withstand higher levels of load (Hansen, 2004). Grain refinement can be achieved via severe plastic deformation (SPD) techniques such as high-pressure torsion (HPT), equal-channel angular pressing (ECAP), accumulative roll bonding (ARB), repetitive corrugation and straightening (RCS) and variations (Azushima et al., 2008; Jahedi et al., 2017a; Segal, 2018). Such creation of ultra-fine grain microstructures in metals and alloys results in significant improvement of mechanical properties, particularly strength. Although a significant amount of experimental works has been conducted on the evolution of grain size in the last couple decades, especially in the area of SPD involving processes such as ECAP and HPT, very little of works are available in the concomitant texture and grain size evolution modeling (Beyerlein and Tóth, 2009).

Mean-field modes such as a viscoplastic self-consistent (VPSC) model (Lebensohn and Tomé, 1993; Molinari et al., 1987) are suitable for

* Corresponding author. Department of Mechanical Engineering, University of New Hampshire, 33 Academic Way, Kingsbury Hall, W119, Durham, NH, 03824, USA.
E-mail address: marko.knezevic@unh.edu (M. Knezevic).

https://doi.org/10.1016/j.mechmat.2024.105212
Received 5 September 2024; Received in revised form 21 November 2024; Accepted 25 November 2024
Available online 26 November 2024

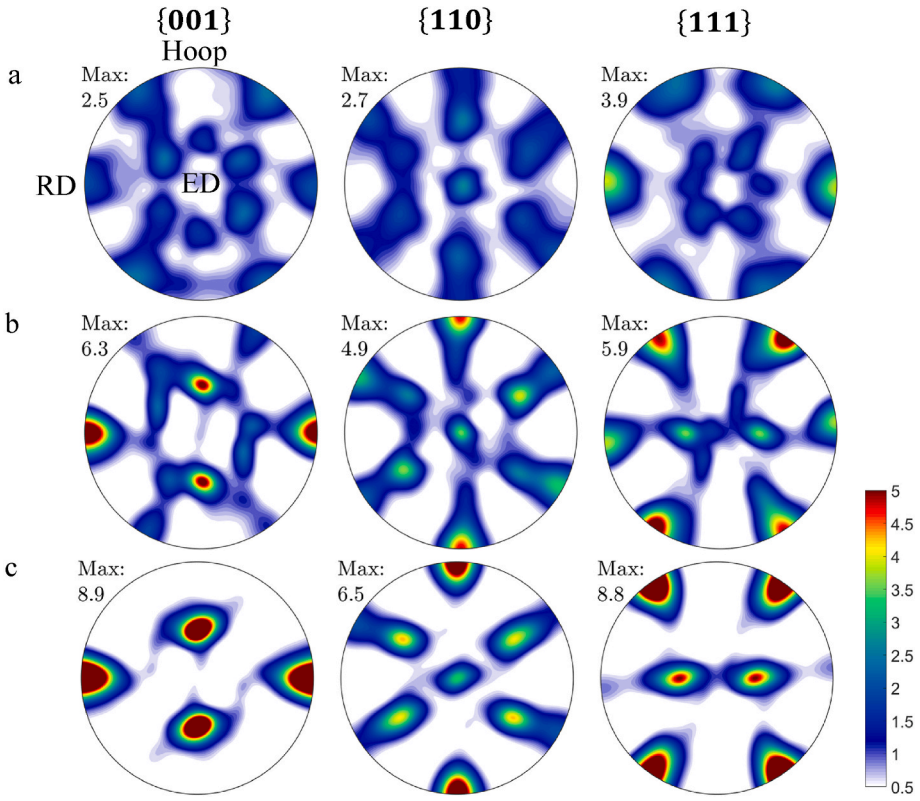

Fig. 1. Stereographic pole figures showing (a) an initial texture of the extruded and annealed 99.99% pure Cu used in simulations, (b) simulated texture after 2 HPT turns, and (c) simulated texture after 4 HPT turns. The radial direction (RD) is along the east, hoop is along the north, and extrusion direction (ED) is out of plane. The data is taken from (Jahedi et al., 2017b).

Table 1
Parameters for the evolution of slip resistance of Cu.

τ_0^α [MPa]	k_1^s [m^{-1}]	g^α	D^α [MPa]	$\rho^s_{0,for}$ [m^{-2}]	$\rho^\alpha_{0,sub}$ [m^{-2}]	b^α [m]	μ^α [MPa]
5.52	4.6×10^7	0.0125	360	1×10^{11}	1×10^{-1}	2.56×10^{-10}	4.8×10^4

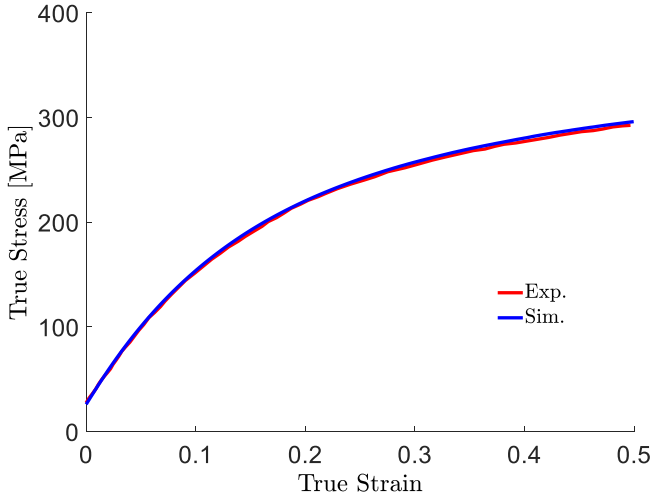

Fig. 2. Comparison of measured and simulated true stress-true strain curve in compression along ED of the extruded and annealed 99.99% pure Cu. The strain rate was 0.001 s^{-1} at T = 298 K.

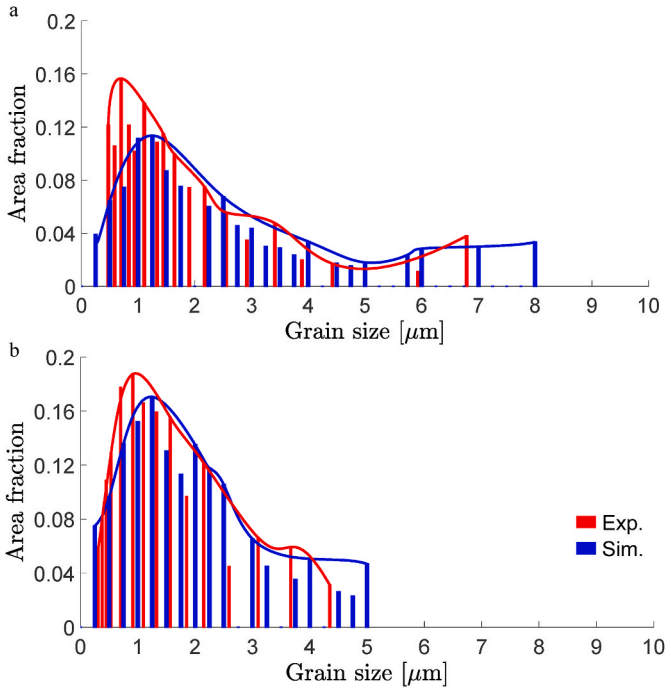

Fig. 3. Comparison of measured and simulated grain size distribution of Cu after (a) 2 HPT turns and (b) 4 HPT turns.

modeling of texture evolution and grain fragmentation while providing a good balance between computational efficiency and accuracy. In contrast, difficulties arise in dealing with geometry of grains in

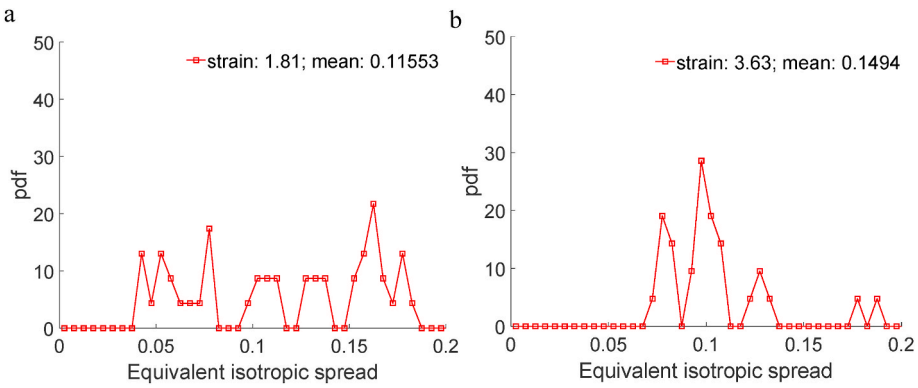

Fig. 4. Probability density of equivalent isotropic spreads in Cu after (a) 2 HPT turns and (b) 4 HPT turns. For reference, the equivalent isotropic spreads correspond to misorientation angles as follows: 0.05 = 9.1°, 0.1 = 18.3°, 0.15 = 27.5°, and 0.2 = 36.7°.

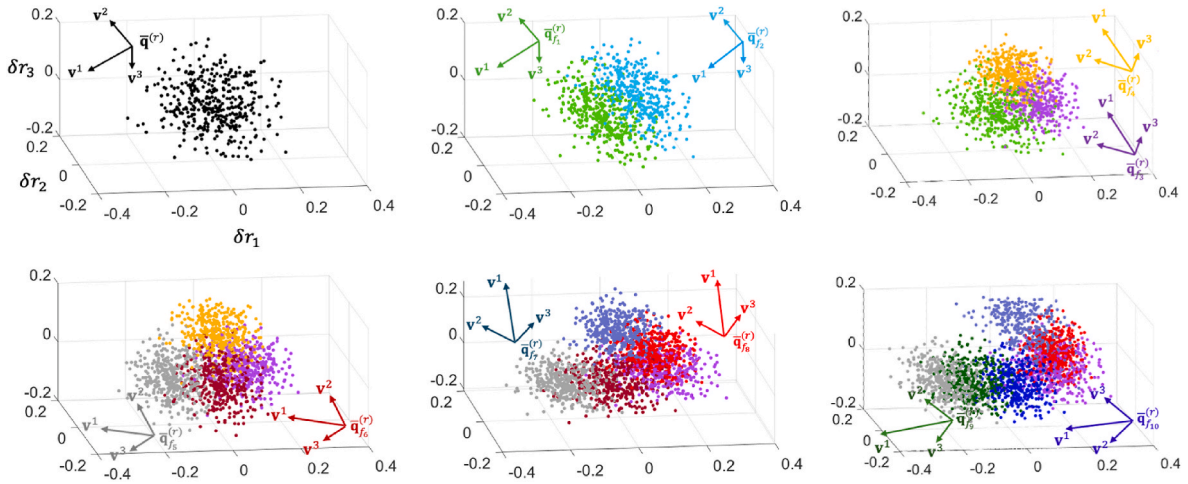

Fig. 5. Discrete representation of the intragranular misorientation spreads, $\langle \delta \mathbf{r} \otimes \delta \mathbf{r} \rangle^{(r)}$, of a randomly selected grain undergoing fragmentation during HPT 2 turns of Cu. The spreads are evolving from a unimodal to a bi-modal distribution with plastic strain. The distributions consist of 400 vector points. The fragmentation occurs along $\mathbf{v}^1$. Mean orientations are indicated. The levels of strain are: 0.75 (parent grain just before the first fragmentation), 0.76 (the parent grain at fragmentation into two child grains each having half of the parent weight), 1.01 (the cyan colored fragment fragments into two children, purple and yellow), 1.09 (four fragments), 1.26 (five fragments), 1.43 (six fragments). No more fragments form after the strain of 1.43–1.81 but only further reorientation to a stronger bi-modal distribution occurs. (For interpretation of the references to color in this figure legend, the reader is referred to the Web version of this article.)

computationally demanding full-field models like crystal plasticity finite element (CPFE) (Feather et al., 2020; Knezevic et al., 2014a; Roters et al., 2010; Sun et al., 2022; Weiss and Knezevic, 2024) and elasto-viscoplastic fast Fourier transform (EVPFFT) formulations (Eghtesad et al., 2020, 2022; Eghtesad and Knezevic, 2020, 2021; Lebensohn et al., 2008, 2012). Nevertheless, coupled EVPFFT/CPFE with a probabilistic cellular automata (CA) approaches to model dynamic recrystallization have been successfully pursued (Nagra et al., 2020; Popova et al., 2015) revealing the role of extension twinning in AZ31 alloy on recrystallization kinetics (Popova et al., 2016). In a standard VPSC, each grain is an ellipsoidal inclusion within a matrix (homogeneous effective medium, HEM) that has the averaged properties over the constituent grains. The properties of HEM are calculated by the self-consistent (SC) linearization scheme which uses the first moments i.e. the average values of micromechanical fields (Lebensohn and Tomé, 1993; Zecevic et al., 2018a; Zecevic and Knezevic, 2019). The state of each grain/inclusion is described by the mean values of the micromechanical fields (strain rate, stress), and microstructural features (crystal orientation, ellipsoidal shape), which evolve with plastic deformation. The standard VPSC does not calculate intragranular misorientation spreads developing in the grains as deformation accumulates (Winther et al., 2017). Owing to the orientation of each grain described only by mean orientation, VPSC tends to predict sharper deformation texture evolution than in measurements or predicted by full-field models (Zecevic et al., 2018b).

VPSC was extended to consider stress and lattice rotation rate fluctuations inside grains to calculate intragranular misorientation spreads (Lebensohn et al., 2007, 2016). The development of such higher order VPSC formulation started from the works reported in the areas of composites (Ponte Castañeda, 2002a,b), which were then adapted to polycrystalline materials (Das and Ponte Castañeda, 2021; Liu and Ponte Castañeda, 2004; Song and Ponte Castañeda, 2018). Accounting for the intragranular misorientation spreads in VPSC allowed for modeling of grain fragmentation to improve the predictions of deformation texture evolution and grain nucleation during recrystallization to enable the predictions of recrystallization texture (Zecevic et al., 2019). Grain boundary and transition bands nucleation mechanisms were conveniently defined based on the available intragranular misorientation spreads (Dillamore and Katoh, 1974; Humphreys and Hatherly, 2004a; Ridha and Hutchinson, 1982). This paper is the first report into predicting concomitant evolution of texture and grain size distributions during deformation and recrystallization relying on the intragranular misorientation spreads in VPSC. We advance the formulation to predict the actual distributions of not only texture but also grain size. However, the current approach cannot directly capture the evolution of grain boundaries i.e. the increase in high-angle grain boundaries.

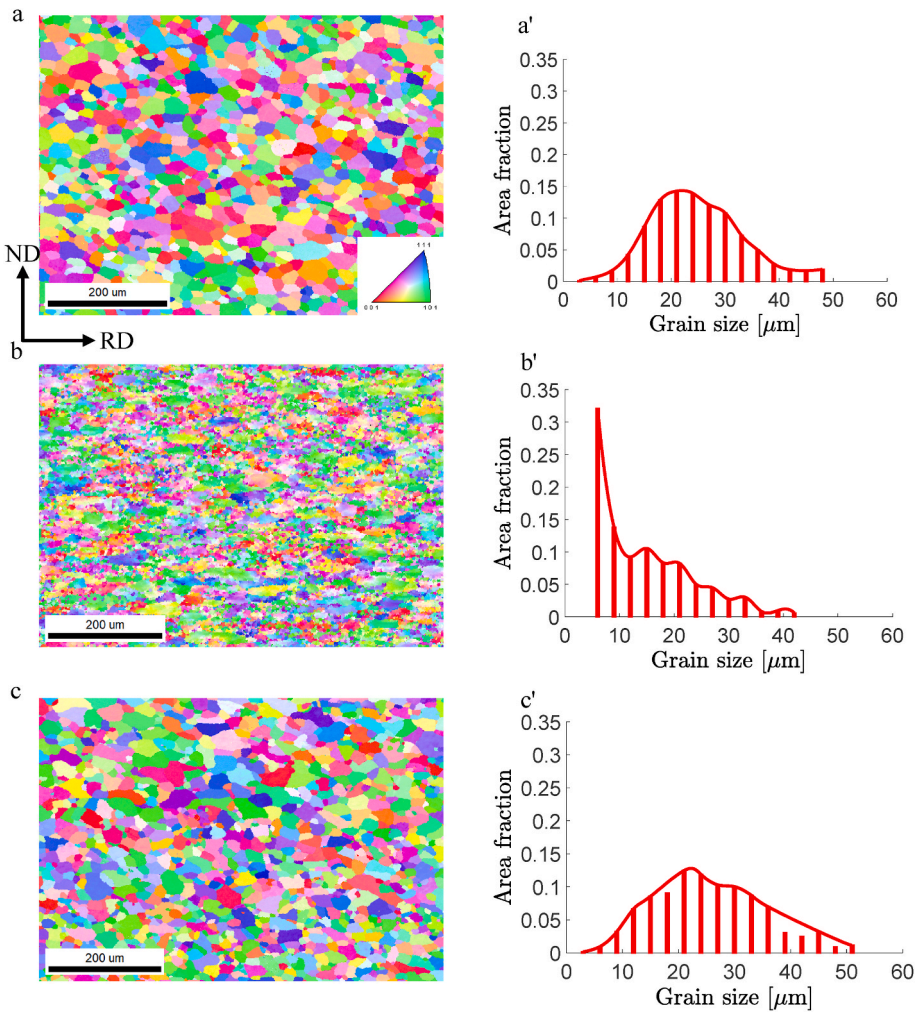

Fig. 6. IPF maps of (a) as-received alloy, (b) structure after CBT to 0.45 strain, (c) structure after subsequent recrystallization. (a' – c') corresponding grain size distributions. The scans were in the middle of the sheet but covered most of the sheet thickness. The data is taken from (Mayer et al., 2024).

Nevertheless, some descriptions of the spatial correlation of mean orientations and their intragranular misorientation spreads can be introduced.

Mean-field models were employed to model texture evolution at very large strains in HPT. However, satisfactory simulation results were not obtained with models that ignore the effect of grain fragmentation (Naghdy et al., 2016). Modeling of grain fragmentation has been attempted within the mean-field modeling frameworks (Beyerlein et al., 2003; Butler and McDowell, 1998; Kumar and Mahesh, 2013; Ostapovets et al., 2012; Toth et al., 2010). While these works reported the reductions in grain size and the increases in high-angle boundaries with plastic strains, the approaches did not rely on the intragranular field fluctuations as the driving force for the fragmentation.

In this paper, the recent formulation termed field fluctuations (FF)-VPSC (Riyad and Knezevic, 2023) is extended to predict not only the evolution of texture in polycrystalline metals undergoing deformation and recrystallization but also the evolution of grain size at high strains. The formulation calculates the second moments of intragranular stresses, the second moments of lattice rotation rates based on the second moment of stress, and the intragranular misorientation spreads based on the second moments of lattice rotation rates. The formulation incorporates grain fragmentation and recrystallization models conceived based on the intragranular misorientation spreads. The novel feature of the model pertains to the calculation of grain size distributions during deformation and recrystallization. The advanced FF-VPSC model is applied to simulate the evolutions of textures and grain size distributions of commercially pure Cu undergoing SPD in HPT. The predictions were in good agreement with corresponding experimental data taken from (Jahedi et al., 2017b). Modeling of grain fragmentation based on intragranular misorientation spreads was the key to accurately predicting the evolution of grain size during HPT. The evolution of texture and grain size in an aluminum alloy (AA) 5182-O after simple tension and static recrystallization are predicted next for further comparisons. These predictions are compared with experimental data presented in (Mayer et al., 2024). Finally, the predictions of texture and grain size distributions in a magnesium alloy WE43 undergoing a thermo-mechanical loading in the dynamic recrystallization regime are presented and compared with the experimental data taken from (Jahedi et al., 2018a, 2018b). After validation, the model is coupled with the implicit finite element method (FEM) via a user-material subroutine (UMAT) in Abaqus to facilitate modeling of complex boundary conditions and geometries. The multilevel approach is referred to as FE-FF-VPSC in which every integration point embeds the FF-VPSC constitutive law, considering texture evolution and the directionality of deformation mechanisms operating at the single crystal level. FE-FF-VPSC is applied to simulate texture evolution during a sequence of rolling, recrystallization, and deep drawing of a circular cup of AA6022-T4. The 50% rolling reduction simulation predicted the through-thickness texture gradient in AA6022-T4. The rolled texture was then recrystallized fully and partially. The texture gradient after rolling, the two texture gradients after rolling followed by recrystallization, and a random texture were used to initialize deep-drawing of a

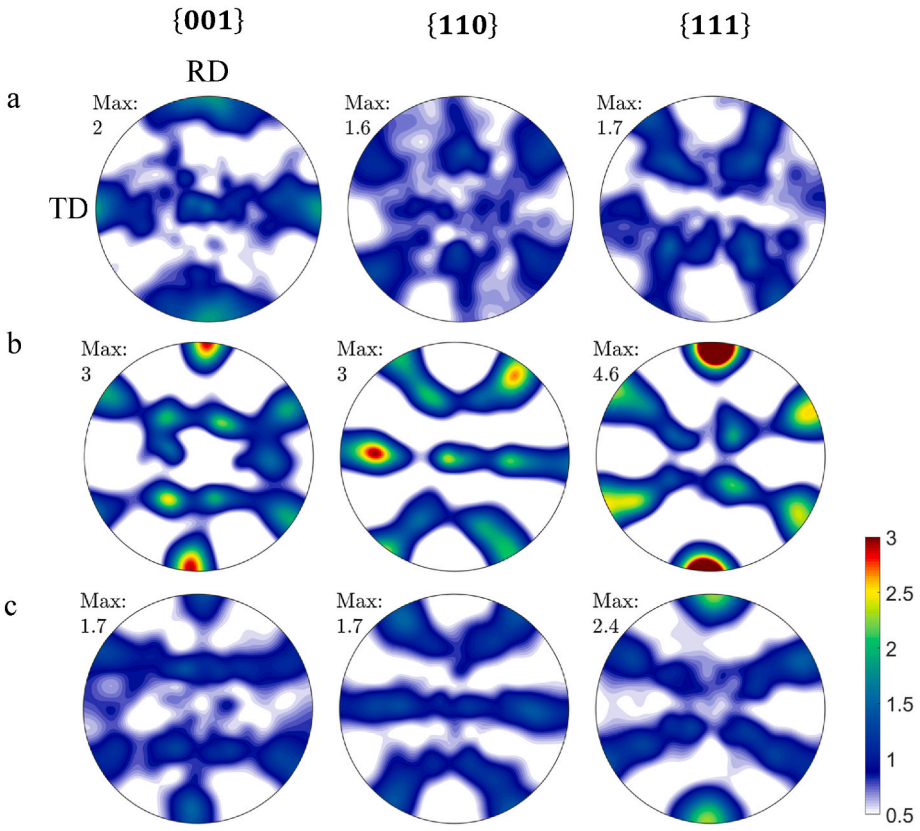

Fig. 7. Stereographic pole figures of AA5182-O showing (a) measured initial texture of as-received alloy used in the simulations, (b) measured texture after tension to 0.45 strain, and (c) measured texture after subsequent full recrystallization.

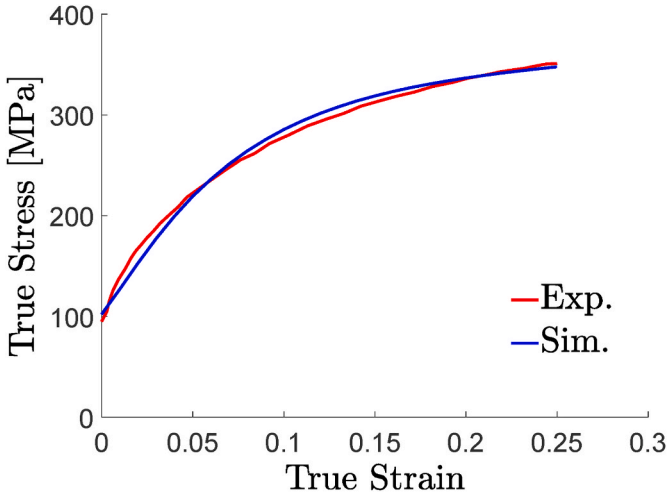

Fig. 8. Comparison of measured and simulated quasi-static true stress-true strain curve of AA5182-O in simple tension along RD at room temperature.

Table 2
Parameters for the evolution of slip resistance of AA5182-O.

τ_0^α [MPa]	k_1^s [m^{-1}]	g^α	D^α [MPa]	$\rho_{0,for}^s$ [m^{-2}]	$\rho_{0,sub}^\alpha$ [m^{-2}]	b^α [m]	μ^α [MPa]
28	1.16×10^8	0.016	300	1×10^{12}	1×10^{-1}	2.56×10^{-10}	4.8×10^4

cylindrical cup simulations. As one of the major defects that occurs in the circular cup deep drawing process is known as earing, the performed simulations allowed for the discussion of the effects of initial textures and underlying anisotropy on the formation of earing profiles during deep drawing. Predicting such geometrical shape changes is important for the optimization of metal forming processes.

2. Modeling framework

This section presents a summary of the standard VPSC formulation (Lebensohn and Tomé, 1993) followed by a summary of the FF-VPSC formulation to calculate the second moment of stress, spin, and intra-granular misorientation spreads (Lebensohn et al., 2007, 2016; Zecevic et al., 2017). The FF-VPSC model remains rigid viscoplastic meaning that the elasticity is neglected. Also, the model remains formulated within the realm of small strains. The grain size evolution calculations facilitated by the grain fragmentation model are described next. Finally, the coupling of the FF-VPSC incorporating the grain fragmentation and recrystallization models with Abaqus via a user-material subroutine (UMAT) is described based previous works (Zecevic et al., 2016a; Zecevic and Knezevic, 2018).

The adopted notations in our descriptions are as follows. Tensors are denoted by bold letters, while scalars and tensor components are represented by italic format and not bold. The outer product of two tensors is represented by "$\otimes$", while the inner products between two vectors or tensors are represented by "." (summation over one contracted index), ":" (summation over two contracted indices) and "" (summation over four contracted indices).

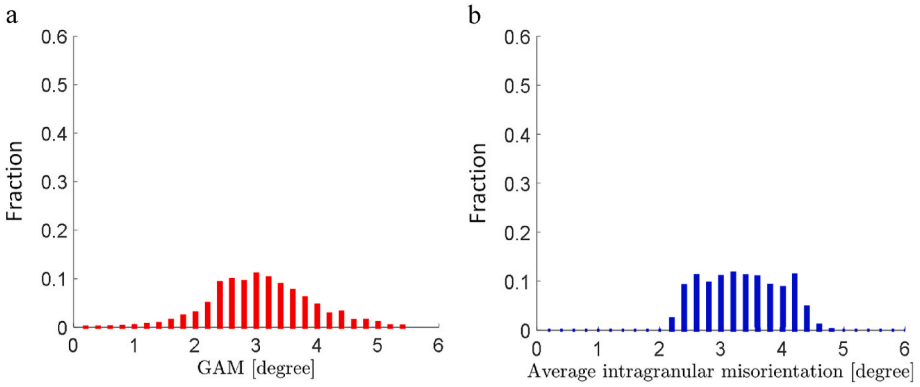

Fig. 9. Normalized distributions of (a) GAM spreads measured after CBT at a strain of 0.45 and (b) corresponding predicted average intragranular misorientation spreads using Eq. (A1).

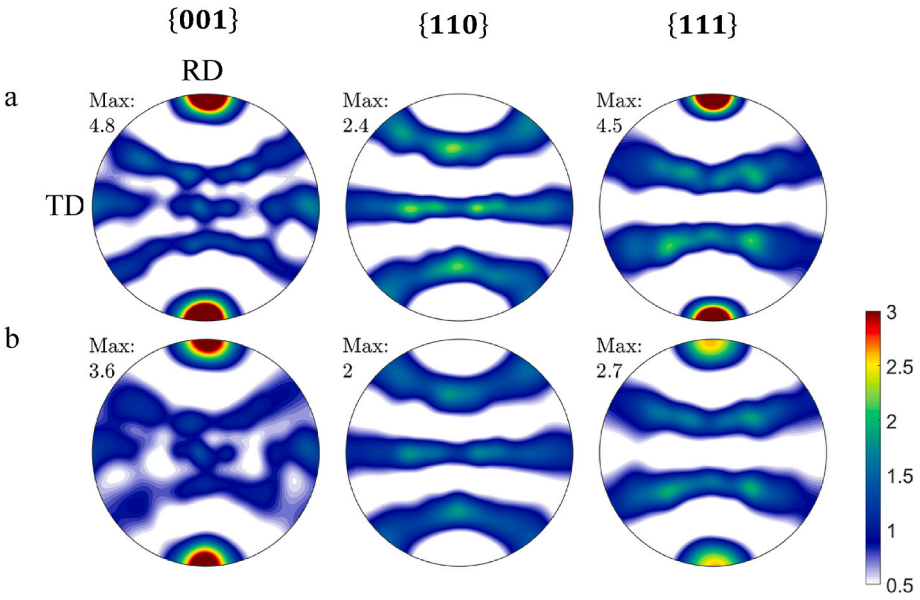

Fig. 10. Stereographic pole figures showing (a) predicted deformed texture at a true strain of 0.45 after tension along RD and (b) predicted fully recrystallized texture for of AA5182-O.

Table 3
Recrystallization model parameters for AA5182-O.

Grain boundary nucleation				Transition band nucleation				Grain growth
E_{th}^{gb}	$\delta\theta_{th}^{gb}$	A_{gb}	B_{gb}	E_{th}^{tb}	$\delta\theta_{th}^{tb}$	A_{tb}	B_{tb}	M
0.0	1.5×10^{-3}	3.5×10^{-4}	3.5×10^{-7}	0.0	N/A	N/A	N/A	1.5×10^{-9}

2.1. Standard VPSC formulation: constitutive and homogenization equations

The constitutive relation between the viscoplastic strain rate (the symmetric part of the traceless velocity gradient), $\dot{\varepsilon}$ and the deviatoric part of the Cauchy stress tensors, σ at a single crystal material point **x** is given by the following constitutive equation:

$$\dot{\boldsymbol{\varepsilon}}(\mathbf{x}) = \sum_s \dot{\gamma}^s(\mathbf{x})\mathbf{m}^s(\mathbf{x}) = \dot{\gamma}_0 \sum_s \left(\frac{|\boldsymbol{\sigma}(\mathbf{x}) : \mathbf{m}^s(\mathbf{x})|}{\tau_c^s(\mathbf{x})}\right)^n \text{sign}(\boldsymbol{\sigma}(\mathbf{x}) : \mathbf{m}^s(\mathbf{x}))\mathbf{m}^s(\mathbf{x}) \tag{1}$$

where $\dot{\gamma}^s(\mathbf{x}) = \dot{\gamma}_0 \left(\frac{|\tau^s(\mathbf{x})|}{\tau_c^s(\mathbf{x})}\right)^n \text{sign}(\tau^s(\mathbf{x}))$ is the shear rate of slip system s at the material point **x**. $\mathbf{m}^s(\mathbf{x}) = \frac{1}{2}(\mathbf{b}^s(\mathbf{x}) \otimes \mathbf{n}^s(\mathbf{x}) + \mathbf{n}^s(\mathbf{x}) \otimes \mathbf{b}^s(\mathbf{x}))$ is the symmetric Schmid tensor of the slip system s; $\mathbf{n}^s$ and $\mathbf{b}^s$ are the slip plane normal and the normalized Burgers vector to a unit vector, respectively of slip system s. $\dot{\gamma}_0$ is the reference shear rate, the value of which is taken

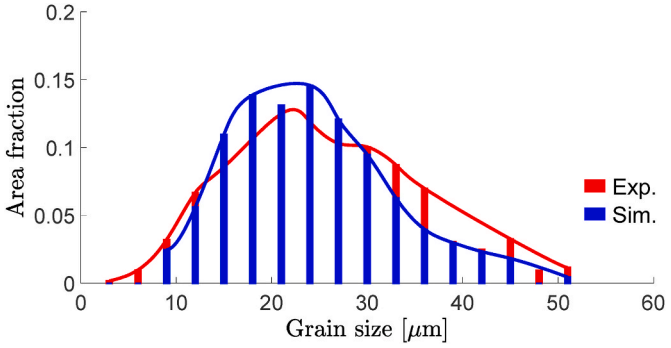

Fig. 11. Comparison of measured and simulated grain size distributions after tension to 0.45 true strain along RD and subsequent recrystallization of AA5182-O.

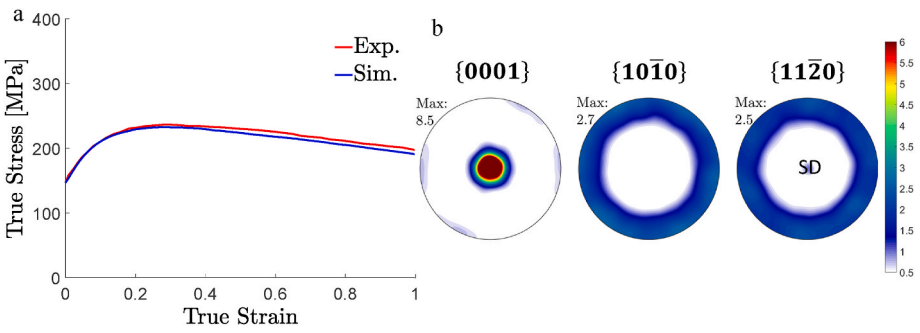

Fig. 12. (a) Comparison of measured and simulated true stress-true strain curves of as-cast alloy WE43 in compression at 550 K under the dynamic recrystallization regime and strain rate of 0.01 s^{-1} along the solidification direction (SD) and (b) predicted deformed and recrystallized texture. The data is taken from (Jahedi et al., 2018a).

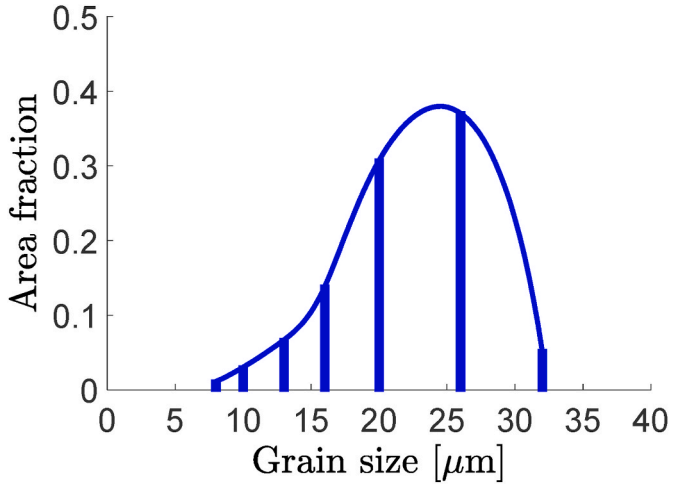

Fig. 13. Simulated grain size distribution in alloy WE43 after compression to 1.0 true strain at a temperature of T = 550 K under the dynamic recrystallization regime.

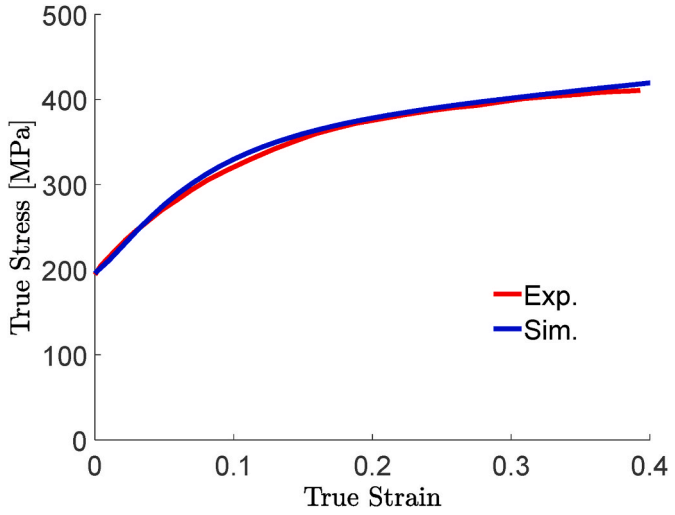

Fig. 14. Comparison of measured (Knezevic et al., 2019) and simulated true stress-true strain response of AA6022-T4 in quasi-static tension at room temperature.

to be 1 s^{-1} in all our calculations. The resolved shear rate on slip system s, $\tau^s(\mathbf{x})$ is defined as $\tau^s(\mathbf{x}) = \mathbf{m}^s(\mathbf{x}) : \boldsymbol{\sigma}(\mathbf{x})$. The inverse of strain rate sensitivity, n, is taken as 20 for all the simulation cases. The form of Eq. (1) along with the exponent $n = 20$ is sufficient to provide uniqueness of solutions for the active slip systems that accommodate imposed plastic strain rates but not to reflect material strain rate sensitivity. Modeling realistic material strain rate-sensitivity exponents within out crystal visco-plasticity model is possible (Knezevic et al., 2016b) but that is not an objective of the present work. τ_c^s is the critical resolved shear stress on slip system s. A hardening law for the evolution of τ_c^s is provided in Appendix A.

Table 4
Parameters for the evolution of slip resistance of AA6022-T4. The crystal stiffness constants are $C_{11} = 108.2$ GPa, $C_{12} = 61.3$ GPa, and $C_{44} = 28.5$ GPa (Meyers and Chawla, 2008).

τ_0^α [MPa]	k_1^s [m^{-1}]	g^α	D^α [MPa]	$\rho_{0,for}^s$ [m^{-2}]	$\rho_{0,sub}^\alpha$ [m^{-2}]	b^α [m]	μ^α [MPa]
68	6.8×10^7	0.016	180	1×10^{11}	1×10^{-1}	2.56×10^{-10}	4.8×10^4

Eq. (1) can be linearized at the grain level as follows:

$$\dot{\boldsymbol{\varepsilon}}(\mathbf{x}) = \mathbf{M}^{(r)} : \boldsymbol{\sigma}(\mathbf{x}) + \dot{\boldsymbol{\varepsilon}}^{0(r)}, \tag{2}$$

where $\dot{\boldsymbol{\varepsilon}}^{0(r)}$ and $\mathbf{M}^{(r)}$ are the back-extrapolated strain rate and linearized compliance respectively for grain r, the formulation of which are dependent on the linearization method chosen. For this paper, affine linearization scheme (Masson et al., 2000) is adopted. The affine linearization scheme defines these moduli as follows:

$$\mathbf{M}^{(r)} = n\dot{\gamma}_0 \sum_s \frac{\mathbf{m}^{s(r)} \otimes \mathbf{m}^{s(r)}}{\tau_c^{s(r)}} \left(\frac{\mathbf{m}^{s(r)} : \boldsymbol{\sigma}^{(r)}}{\tau_c^{s(r)}} \right)^{n-1} \tag{3}$$

$$\dot{\boldsymbol{\varepsilon}}^{0(r)} = (1-n)\dot{\gamma}_0 \sum_s \left(\frac{\mathbf{m}^{s(r)} : \boldsymbol{\sigma}^{(r)}}{\tau_c^{s(r)}} \right)^n \operatorname{sign}\left(\mathbf{m}^{s(r)} : \boldsymbol{\sigma}^{(r)} \right) \tag{4}$$

At macroscopic level (grain aggregate), we can get a linear relationship analogous to Eq. (2) as:

$$\dot{\mathbf{E}} = \overline{\mathbf{M}} : \boldsymbol{\Sigma} + \dot{\mathbf{E}}^0, \tag{5}$$

where $\overline{\mathbf{M}}$ is the macroscopic viscoplastic compliance; $\dot{\mathbf{E}}$ and $\boldsymbol{\Sigma}$ are the macroscopic strain rate and stress respectively; and $\dot{\mathbf{E}}^0$ is the back-extrapolated strain rate. The macroscopic properties of Eq. (5) are given by the self-consistent equations as:

$$\overline{\mathbf{M}} = \langle \mathbf{M}^{(r)} : \mathbf{B}^{(r)} \rangle : \langle \mathbf{B}^{(r)} \rangle^{-1}, \tag{6}$$

$$\dot{\mathbf{E}}^0 = \langle \mathbf{M}^{(r)} : \mathbf{b}^{(r)} + \dot{\boldsymbol{\varepsilon}}^{0(r)} \rangle - \langle \mathbf{M}^{(r)} : \mathbf{B}^{(r)} \rangle : \langle \mathbf{B}^{(r)} \rangle^{-1} : \langle \mathbf{b}^{(r)} \rangle, \tag{7}$$

where $\langle\rangle$ represents volume average. $\mathbf{B}^{(r)}$ and $\mathbf{b}^{(r)}$ are the stress locali-

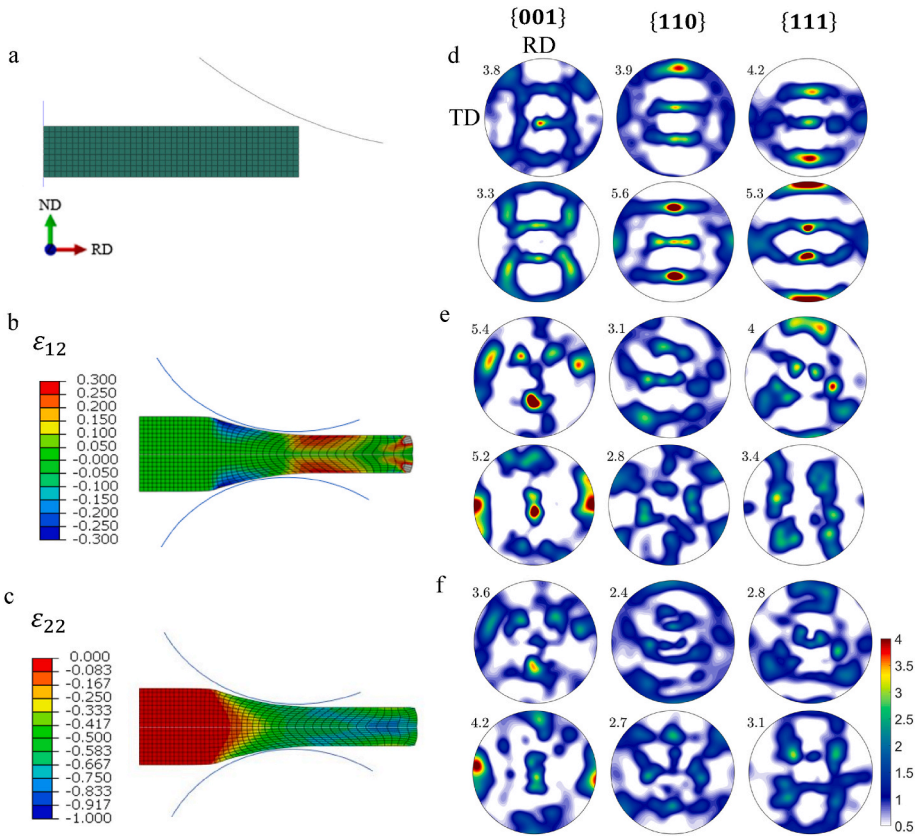

Fig. 15. (a) Rolling simulation setup created in Abaqus in which the rollers impart a reduction of 50% over the initial mesh in 2D. The half-model sheet consists of 396 CPE4 plane strain elements. (b) Logarithmic shear strain fields developing during the simulation. (c) Logarithmic reduction strain fields developing during the simulation. (d) Pole figures showing texture after rolling near the surface of the sheet (top) and in the middle of the sheet (bottom). (e) Pole figures showing fully recrystallized textures near the surface of the sheet (top) and in the middle of the sheet (bottom). (f) Pole figures showing partially recrystallized textures near the surface of the sheet (top) and in the middle of the sheet (bottom). 1 = X = RD (rolling direction) and 2 = Y=ND (normal direction).

Table 5
Recrystallization model parameters for AA6022-T4.

Grain boundary nucleation				Transition band nucleation				Grain growth
E_{th}^{gb}	$\delta\theta_{th}^{gb}$	A_{gb}	B_{gb}	E_{th}^{tb}	$\delta\theta_{th}^{tb}$	A_{tb}	B_{tb}	M
N/A	N/A	N/A	N/A	0.0	1.0×10^{-3}	5.2×10^{-4}	3.1×10^{-6}	1.5×10^{-9}

zation tensors given as functions of the microscopic and macroscopic moduli and are expressed as:

$$\mathbf{B}^{(r)} = (\mathbf{M}^{(r)} + \widetilde{\mathbf{M}})^{-1} : (\overline{\mathbf{M}} + \widetilde{\mathbf{M}}), \tag{8}$$

$$\mathbf{b}^{(r)} = \left(\mathbf{M}^{(r)} + \widetilde{\mathbf{M}}\right)^{-1} : \left(\dot{\mathbf{E}}^{0} - \dot{\boldsymbol{\varepsilon}}^{0(r)}\right). \tag{9}$$

The self-consistent equations are solved numerically by a fix-point method since they are implicit in the macroscopic moduli, $\overline{\mathbf{M}}$ and $\dot{\mathbf{E}}^{0}$. In the self-consistent scheme, each grain is considered an ellipsoidal inhomogeneity embedded in HEM. The field values of the inhomogeneity represented as grain can be obtained by Eshelby's inclusion approach (Eshelby and Peierls, 1997).

The interaction equation relating the deviations in stress, $\widetilde{\boldsymbol{\sigma}}^{(r)}$ and strain rate, $\widetilde{\dot{\boldsymbol{\varepsilon}}}^{(r)}$ of the inclusion with respect to the macroscopic values is given by:

$$\widetilde{\dot{\boldsymbol{\varepsilon}}}^{(r)} = -\widetilde{\mathbf{M}} : \widetilde{\boldsymbol{\sigma}}^{(r)}, \tag{10}$$

where $\widetilde{\mathbf{M}} = (\mathbf{I} - \mathbf{S})^{-1} : \mathbf{S} : \overline{\mathbf{M}}$ is the interaction tensor and $\mathbf{S}$ is the symmetric Eshelby tensor.

After convergence of the affine linearization, the slip system shearing rates $\dot{\gamma}^{s}$ are used to calculate lattice spin $\dot{\boldsymbol{\omega}}$ for the evolution of texture, which is expressed as:

$$\dot{\boldsymbol{\omega}}^{(r)} = \dot{\boldsymbol{\omega}}^{app} + \boldsymbol{\Pi}^{(r)} - \dot{\boldsymbol{\omega}}^{p(r)}, \tag{11}$$

where $\dot{\boldsymbol{\omega}}^{app}$ is the macroscopic imposed spin over the aggregate, $\boldsymbol{\Pi}$ is the antisymmetric part Eshelby tensor, and $\dot{\boldsymbol{\omega}}^{p}$ is the plastic spin owing to slip, which is obtained via:

$$\dot{\boldsymbol{\omega}}^{p} = \frac{1}{2}\sum_{s}\dot{\gamma}^{s}(\mathbf{b}^{s}(\mathbf{x}) \otimes \mathbf{n}^{s}(\mathbf{x}) - \mathbf{n}^{s}(\mathbf{x}) \otimes \mathbf{b}^{s}(\mathbf{x})). \tag{12}$$

2.2. Stress, lattice rotation rate, and intragranular misorientation fluctuations

The second moments of stress for each grain at time t are calculated as (Lebensohn et al., 2007):

$$\begin{aligned}\langle \boldsymbol{\sigma}^{t} \otimes \boldsymbol{\sigma}^{t} \rangle^{(r)} &= \frac{2}{w^{t(r)}} \frac{\partial \widetilde{U}_{T}^{t}}{\partial \mathbf{M}^{t(r)}} \\ &= \frac{1}{w^{t(r)}} \frac{\partial \overline{\mathbf{M}}^{t}}{\partial \mathbf{M}^{t(r)}} :: (\boldsymbol{\Sigma}^{t} \otimes \boldsymbol{\Sigma}^{t}) + \frac{2}{w^{t(r)}} \frac{\partial \dot{\mathbf{E}}^{0t}}{\partial \mathbf{M}^{t(r)}} : \boldsymbol{\Sigma}^{t} + \frac{1}{w^{t(r)}} \frac{\partial \overline{G}^{t}}{\partial \mathbf{M}^{t(r)}},\end{aligned} \tag{13}$$

where $\widetilde{U}_{T}^{t}$ is the effective stress potential, and $\overline{G}^{t}$ is the energy under zero applied stress, which are expressed as:

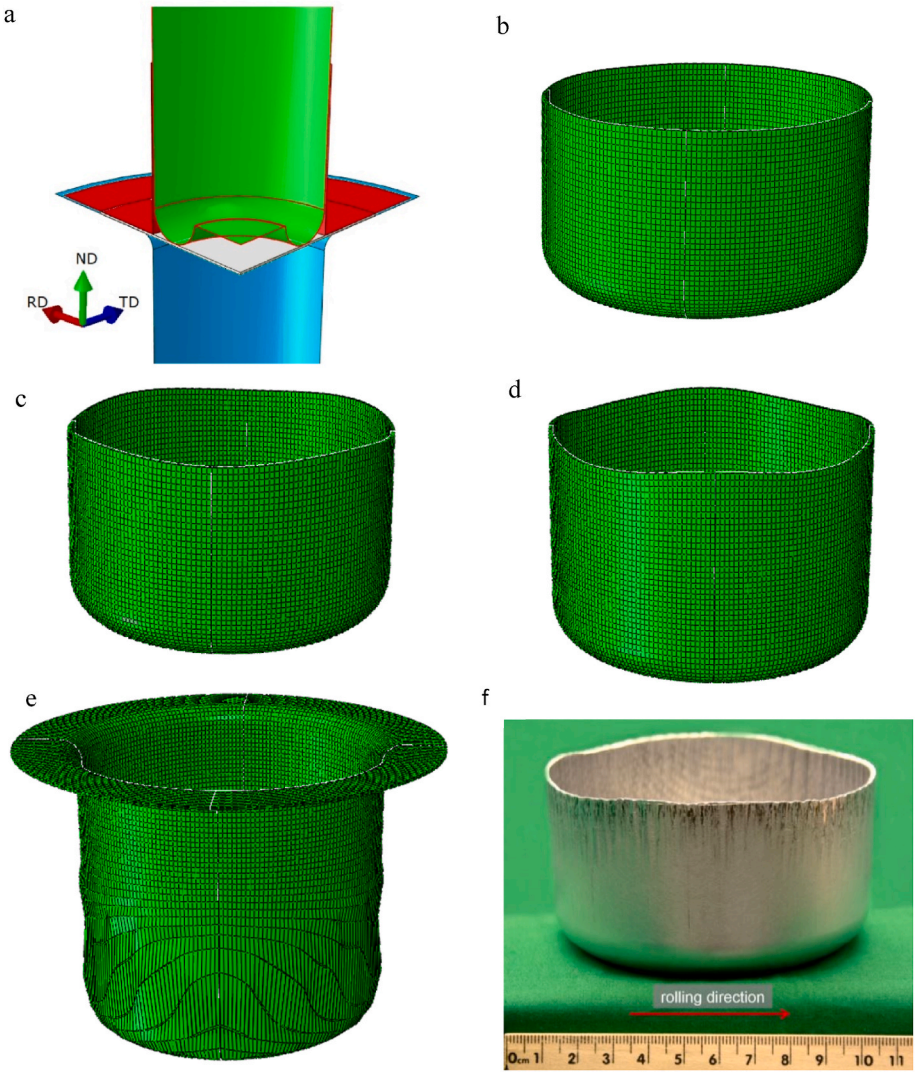

Fig. 16. (a) Cup drawing simulation setup created in Abaqus with mesh of the blank consisting of 14,564C3D8R elements with 4 elements in the through-thickness direction. FE meshes after forming using (b) random texture, (c) rolled texture, (d) partially recrystallized texture, and (e) fully recrystallized texture. (f) Photograph of an experimentally formed cup of the alloy taken from (Tian et al., 2017).

$$\widetilde{U}_T^t = \frac{1}{2}\overline{\mathbf{M}}^t :: (\boldsymbol{\Sigma}^t \otimes \boldsymbol{\Sigma}^t) + \dot{\mathbf{E}}^{0t} : \boldsymbol{\Sigma}^t + \frac{1}{2}\overline{G}^t, \tag{14}$$

$$\overline{G}^t = \sum\nolimits_r w^{t(r)} \dot{\boldsymbol{\varepsilon}}^{0t(r)} : \mathbf{b}^{t(r)}, \tag{15}$$

where $w^{t(r)}$ is the volume fraction of grain r.

We express the orientation at any point $\mathbf{x}$ of a grain by quaternion $\mathbf{q}^t(\mathbf{x})$ or equivalently by its three independent vector quantities denoted by $\delta\mathbf{r}^t(\mathbf{x})$.

Intragranular stress fluctuations owing to the spatial variation of intragranular mean properties $\delta\boldsymbol{\sigma}^{t(\overline{q})}(\mathbf{x})$ and intragranular misorientations field $\delta\boldsymbol{\sigma}^{t(\delta r)}(\mathbf{x})$ alter the mean stress of the grain $\boldsymbol{\sigma}^{t(r)}$ at a material point $\mathbf{x}$ at time t as:

$$\boldsymbol{\sigma}^t(\mathbf{x}) = \boldsymbol{\sigma}^{t(r)} + \delta\boldsymbol{\sigma}^{t(\overline{q})}(\mathbf{x}) + \delta\boldsymbol{\sigma}^{t(\delta r)}(\mathbf{x}). \tag{16}$$

The second moment of stress in a grain r then can be expressed as:

$$\begin{aligned}\langle \boldsymbol{\sigma}^t \otimes \boldsymbol{\sigma}^t \rangle^{(r)} = {} & \boldsymbol{\sigma}^{t(r)} \otimes \boldsymbol{\sigma}^{t(r)} + \langle \delta\boldsymbol{\sigma}^{t(\overline{q})} \otimes \delta\boldsymbol{\sigma}^{t(\overline{q})} \rangle^{(r)} + \langle \delta\boldsymbol{\sigma}^{t(\delta r)} \otimes \delta\boldsymbol{\sigma}^{t(\delta r)} \rangle^{(r)} \\ & + \langle \delta\boldsymbol{\sigma}^{t(\overline{q})} \otimes \delta\boldsymbol{\sigma}^{t(\delta r)} \rangle^{(r)} + \langle \delta\boldsymbol{\sigma}^{t(\delta r)} \otimes \delta\boldsymbol{\sigma}^{t(\overline{q})} \rangle^{(r)}\end{aligned} \tag{17}$$

The evaluation of the second moment terms on the right-side of Eq. (17) is essential for the calculation of intragranular misorientation spreads. The procedures were described in detail in (Riyad et al., 2024; Riyad and Knezevic, 2023; Zecevic et al., 2018b). It is to be noted that, these expressions do not change the second moment of stress $\frac{2}{w^{t(r)}} \frac{\partial \widetilde{U}_T^t}{\partial \mathbf{M}^{t(r)}}$ given in Eq. (13).

After calculating the fluctuations in stress, the lattice rotation rates at a point $\mathbf{x}$ at time t can be similarly expressed after considering stress fluctuations and intragranular misorientations as:

$$\dot{\boldsymbol{\omega}}^t(\mathbf{x}) = \dot{\boldsymbol{\omega}}^{t(r)} + \delta\dot{\boldsymbol{\omega}}^{t(\delta\sigma)}(\mathbf{x}) + \delta\dot{\boldsymbol{\omega}}^{t(\delta r)}(\mathbf{x}), \tag{18}$$

where $\dot{\boldsymbol{\omega}}^{t(r)}$ is the average lattice rotation rate, $\delta\dot{\boldsymbol{\omega}}^{t(\delta\sigma)}(\mathbf{x})$ is the lattice rotation rate fluctuations caused by the stress fluctuations, and $\delta\dot{\boldsymbol{\omega}}^{t(\delta r)}(\mathbf{x})$ is the lattice rotation rate fluctuations by the misorientation fluctuations inside the given grain, r.

Then, the second moments of lattice rotation rates are expressed as:

$$\begin{aligned}\langle \dot{\boldsymbol{\omega}}^t \otimes \dot{\boldsymbol{\omega}}^t \rangle^{(r)} = {} & \dot{\boldsymbol{\omega}}^{t(r)} \otimes \dot{\boldsymbol{\omega}}^{t(r)} + \langle \delta\dot{\boldsymbol{\omega}}^{t(\delta\sigma)} \otimes \delta\dot{\boldsymbol{\omega}}^{t(\delta\sigma)} \rangle^{(r)} + \langle \delta\dot{\boldsymbol{\omega}}^{t(\delta r)} \otimes \delta\dot{\boldsymbol{\omega}}^{t(\delta r)} \rangle^{(r)} \\ & + \langle \delta\dot{\boldsymbol{\omega}}^{t(\delta\sigma)} \otimes \delta\dot{\boldsymbol{\omega}}^{t(\delta r)} \rangle^{(r)} + \langle \delta\dot{\boldsymbol{\omega}}^{t(\delta r)} \otimes \delta\dot{\boldsymbol{\omega}}^{t(\delta\sigma)} \rangle^{(r)}.\end{aligned} \tag{19}$$

Finally, the second moments of misorientation (i.e., the intragranular misorientation spreads) at a time $t + \Delta t$ are:

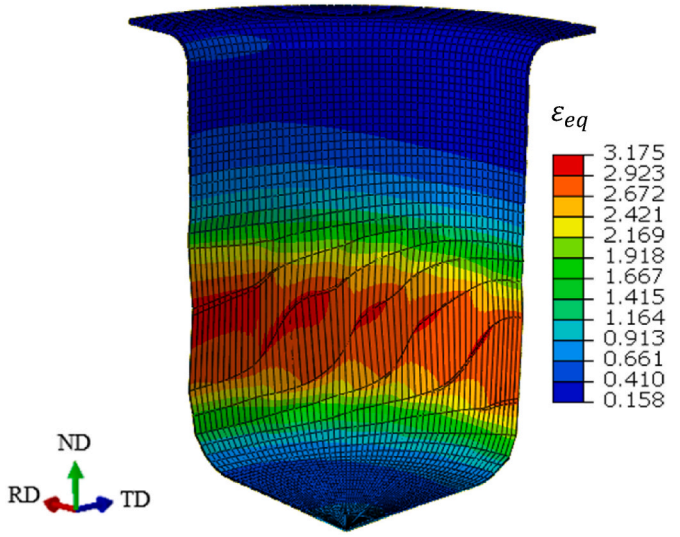

Fig. 17. Equivalent strain contours over the cup drawn with the fully recrystallized texture. The figure shows the necking area with the highest contour intensities.

$$\langle \delta\mathbf{r}^{t+\Delta t} \otimes \delta\mathbf{r}^{t+\Delta t} \rangle^{(r)} = \langle \delta\mathbf{r}^{t}_{inc} \otimes \delta\mathbf{r}^{t}_{inc} \rangle^{(r)} + \langle \delta\mathbf{r}^{t,rot} \otimes \delta\mathbf{r}^{t}_{inc} \rangle^{(r)} + \langle \delta\mathbf{r}^{t}_{inc} \otimes \delta\mathbf{r}^{t,rot} \rangle^{(r)} + \langle \delta\mathbf{r}^{t,rot} \otimes \delta\mathbf{r}^{t,rot} \rangle^{(r)}. \tag{20}$$

The above expressions of the second moments in the right-hand side of Eq. (17), Eq. (19), and Eq. (20) are provided explicitly in (Riyad and Knezevic, 2023; Zecevic et al., 2017, 2018b).

2.3. The evolution of grain size with deformation

At large strains, the misorientation spreads in grains defined by Eq. (20) may become so large that it becomes erroneous to represent the orientation of the grain with just one mean value and 1 s moment. In this case, grain fragmentation becomes necessary. In our formulation, when the misorientation spread of a grain reaches a critical value during deformation, the parent grain is subdivided into two child grains and in the next deformation steps. The fragmented child grains equally split the parent grain into two and are initialized with state variables of the parent. Every parent grain is an ellipsoid evolving its shape during deformation. The geometry of the parent ellipsoid is split along the directions, which will be described shortly, into two child ellipsoids of the same shape as the parent but half the size/weight of the parent. In order to quantify the magnitude of intragranular misorientation spreads, we define an equivalent isotropic spread: $SD = \sqrt[3]{SD_1 \times SD_2 \times SD_3}$, which is a scalar quantity with $SD_i = \sqrt{\lambda^i}$, where λ^i are the principal values with directions, $\mathbf{v}^i$ of the intragranular misorientation distribution, $\langle \delta\mathbf{r} \otimes \delta\mathbf{r} \rangle^{(r)}$ given in Eq. (20).

In order to divide the misorientation distribution of a parent grain described by its mean value, $\langle \delta\mathbf{r} \rangle^{(r)} = 0$ and its second moment, $\langle \delta\mathbf{r} \otimes \delta\mathbf{r} \rangle^{(r)}$ into two equally weighted child distribution, we first calculate the eigenvalues and eigenvectors of the parent's misorientation distribution, $\langle \delta\mathbf{r} \otimes \delta\mathbf{r} \rangle^{(r)}$ and arrange them in descending order as: $\mathbf{E} = [\lambda^1, \lambda^2, \lambda^3]$ and $\mathbf{V} = [\mathbf{v}^1, \mathbf{v}^2, \mathbf{v}^3]$ respectively. In our formulation, when standard deviation SD_1 along the largest principal direction $\mathbf{v}^1$ reaches a critical value, two child grains are created from the parent grain. The mean misorientations of the two child grains relative to the mean orientation of the parent are defined as (Miller and Rice, 1983; Zecevic et al., 2018b):

$$\langle \delta\mathbf{r} \rangle^{(r)}_{f_1} = -2\sqrt{\frac{\lambda^1}{2\pi}}\mathbf{v}^1;\ \langle \delta\mathbf{r} \rangle^{(r)}_{2} = 2\sqrt{\frac{\lambda^1}{2\pi}}\mathbf{v}^1. \tag{21}$$

These misorientations can also be expressed as rotation quaternions:

$$\langle \delta\mathbf{q} \rangle^{(r)}_{f_1} = \begin{Bmatrix} \sqrt{1 - \langle \delta\mathbf{r} \rangle^{(r)}_{f_1} \cdot \langle \delta\mathbf{r} \rangle^{(r)}_{f_1}} \\ \langle \delta\mathbf{r} \rangle^{(r)}_{f_1} \end{Bmatrix};\ \langle \delta\mathbf{q} \rangle^{(r)}_{f_2} = \begin{Bmatrix} \sqrt{1 - \langle \delta\mathbf{r} \rangle^{(r)}_{f_2} \cdot \langle \delta\mathbf{r} \rangle^{(r)}_{f_2}} \\ \langle \delta\mathbf{r} \rangle^{(r)}_{f_2} \end{Bmatrix}. \tag{22}$$

The mean orientations of fragments are then expressed as:

$$\overline{\mathbf{q}}^{(r)}_{f_1} = \langle \delta\mathbf{q} \rangle^{(r)}_{f_1} \overline{\mathbf{q}}^{(r)};\ \overline{\mathbf{q}}^{(r)}_{f_2} = \langle \delta\mathbf{q} \rangle^{(r)}_{f_2} \overline{\mathbf{q}}^{(r)}. \tag{23}$$

Finally, the misorientation spreads of the child grains in the principal frame of parent's spread are given as:

$$\langle \delta\mathbf{r} \otimes \delta\mathbf{r} \rangle^{(r),p}_{f_1} = \langle \delta\mathbf{r} \otimes \delta\mathbf{r} \rangle^{(r),p}_{f_2} = \begin{bmatrix} \lambda^1\left(1 - \frac{2}{\pi}\right) & 0 & 0 \\ 0 & \lambda^2 & 0 \\ 0 & 0 & \lambda^3 \end{bmatrix}. \tag{24}$$

To obtain the misorientation spreads around the child mean orientations in the sample frame, the simple coordinate transformation is applied as:

$$\langle \delta\mathbf{r} \otimes \delta\mathbf{r} \rangle^{(r)}_{f_1} = \langle \delta\mathbf{r} \otimes \delta\mathbf{r} \rangle^{(r)}_{f_2} = \mathbf{V} \langle \delta\mathbf{r} \otimes \delta\mathbf{r} \rangle^{(r),p}_{f_1} \mathbf{V}^T. \tag{25}$$

The intragranular misorientation spreads, $\langle \delta\mathbf{r} \otimes \delta\mathbf{r} \rangle^{(r)}$, and their eigen values and vectors are calculated in each deformation step. When the misorientation along the largest axis $\mathbf{v}^1$, calculated by $\alpha = 4\sin^{-1}\left(2\sqrt{\frac{\lambda^1}{2\pi}}\right)$ becomes more than the critical fragmentation angle (set as 15° or $SD_1 = 0.082$), the parent is divided into 2 child grains, and they are initialized with their parents' filed properties. In the next deformation steps (after the fragmentation), the children evolve independently and might undergo further subdivision if the above criterion becomes satisfied.

The grain size (average diameter) of the fragmented grains can now be calculated for plotting grain size distributions. First, we calculate the total volume of the grains, V_{tot}, either from the initial grains usually set as spherical with their diameters, D_i, or from ellipsoidal grains set initially or evolved during deformation with their a_i representing the major axis and b_i and c_i representing minor axes:

$$V_{tot} = \sum_i \frac{1}{6}\pi {D_i}^3 \text{ or } V_{tot} = \sum_i \frac{1}{6}\pi a_i b_i c_i. \tag{26}$$

The diameter of every grain, $D^{(r)}_g$, assuming it is spherical at any deformation step and can now be calculated from its weight, $w^{(r)}$ using:

$$D^{(r)}_g = 2\left(w^{(r)}\frac{3V_{tot}}{4\pi}\right)^{1/3}. \tag{27}$$

Therefore, the plotted distributions will be based on the spherical grains. The recrystallization model (Zecevic et al., 2019) driven by the intragranular misorientation spreads is briefly summarized in Appendix A. We adopt a dislocation density-based hardening law for the evolution of slip resistance (Beyerlein and Tomé, 2008; Knezevic et al., 2015; Proust et al., 2007). The law is also briefly described the appendix.

2.4. FE-FF-VPSC

FF-VPSC is coupled here with the implicit FEM framework of Abaqus. The response at every material point i.e. integration point of an FE mesh is obtained using FF-VPSC homogenization over an aggregate embedded at the integration point. The VPSC coupling with FEM have been

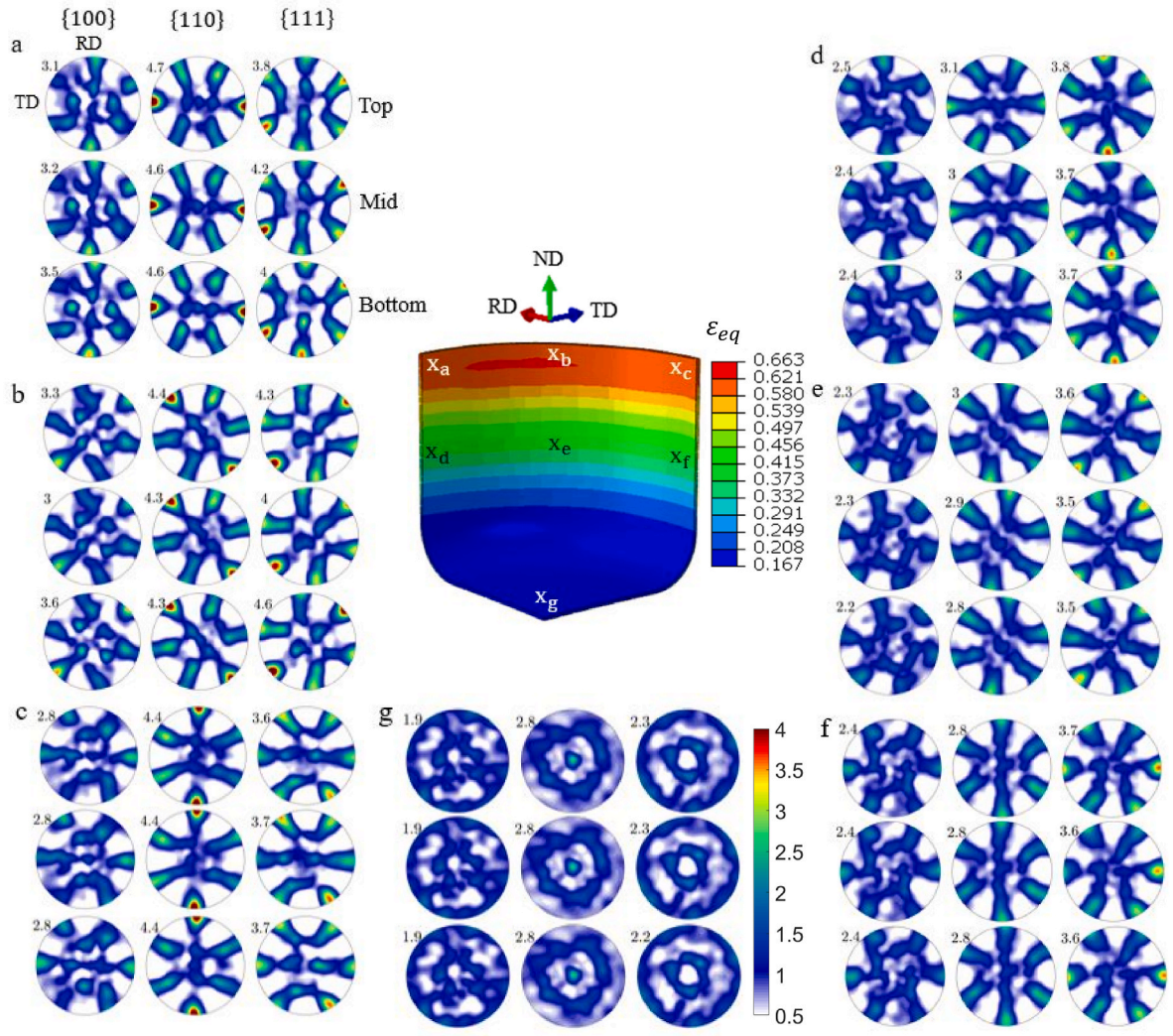

Fig. 18. Equivalent plastic strain contours over the formed cup quarter predicted using FE-FF-VPSC with random initial texture surrounded by sets of pole figures showing texture evolution after forming in the through-thickness direction at top, middle and bottom and at several spatial locations (a) rim along RD, (b) rim along 45°, (c) rim along TD, (d) above punch radius along RD, (e) above punch radius along 45°, (f) above punch radius along TD, and (g) at the center. All pole figures are plotted in their global frame where RD is north, and TD is east.

described in several prior works (Knezevic et al., 2013, 2014b, 2016a; Segurado et al., 2012). The most suitable version for the present work to couple FF-VPSC with FEM is from (Zecevic et al., 2016a). The coupled model is referred to as FE-FF-VPSC.

The formulation of coupling relies on the rate constitutive equation for Cauchy stress rate in the global frame (Asaro, 1979; Asaro and Needleman, 1985; Asaro and Rice, 1977; Hill, 1966; Hill and Rice, 1972; Peirce et al., 1982; Zecevic et al., 2015b, 2015c) as:

$$\dot{\boldsymbol{\Sigma}} = \langle \widehat{\boldsymbol{\sigma}}^{(r)} \rangle + \langle \mathbf{W}^{*(r)}\boldsymbol{\sigma}^{(r)} - \boldsymbol{\sigma}^{(r)}\mathbf{W}^{*(r)} \rangle = \langle \mathbf{C}^{(r)} : \dot{\boldsymbol{\varepsilon}}_{el}^{(r)} \rangle + \langle \dot{\boldsymbol{\omega}}^{(r)}\boldsymbol{\sigma}^{(r)} - \boldsymbol{\sigma}^{(r)}\dot{\boldsymbol{\omega}}^{(r)} \rangle, \tag{28}$$

where $\langle\rangle$ also donates here the volumetric average quantities, $\mathbf{C}^{(r)}$ is the elastic stiffness of a grain r, $\dot{\boldsymbol{\varepsilon}}_{el}^{(r)}$ is the elastic strain rate of a grain r, and $\widehat{\boldsymbol{\sigma}}^{(r)}$ is the Jaumann stress rate of a grain r. The Cauchy stress rate, $\dot{\boldsymbol{\Sigma}}$, is calculated at every integration point as the volume average over inclusions after the integration of Eq. (28). The Cauchy stress rate at the end of a time increment is (Mercier and Molinari, 2009; Zecevic et al., 2016a):

$$\boldsymbol{\Sigma}^{t+\Delta t} = \mathbf{C} : \left(\Delta\mathbf{E}^{FE} - \dot{\mathbf{E}}\Delta t\right) + \langle \Delta\mathbf{R}^{*t,(r)}\boldsymbol{\sigma}^{t,(r)}\Delta\mathbf{R}^{*t,(r)\,T} \rangle, \tag{29}$$

where $\Delta\mathbf{E}^{FE}$ is the total strain increment and Δt is the time increment provided by Abaqus solver, while $\Delta\mathbf{R}^{*t,(r)}$ is the increment in rotation based on $\dot{\omega}^{(r)}$ (Eq. (11)). It is to be noted that $\dot{\mathbf{E}}$ from Eq. (29) is substituted in Eq. (5) in the Newton's solution method (Zecevic et al., 2016a). In addition to stress at each integration point, the Abaqus solver also requires the Jacobian matrix, $\mathbf{J}$. The details can be found in (Zecevic et al., 2016a; Zecevic and Knezevic, 2018).

3. Results and discussion

The FF-VPSC model is applied to predict the evolution of texture and grain size distributions in deformed Cu and deformed and recrystallized AA5182-O and WE43. First, the model is applied to predict the evolution of texture and grain size distributions of commercially pure Cu undergoing SPD in HPT by shear deformation. The predictions are compared with corresponding data from (Jahedi et al., 2017b). Next, the texture and grain size evolution are predicted for deformed and recrystallized AA5182-O and the results are compared with corresponding experimental data taken from (Mayer et al., 2024). Finally, the texture and grain size distribution of an as-cast alloy WE43 are predicted in compression at high temperature in the dynamic recrystallization

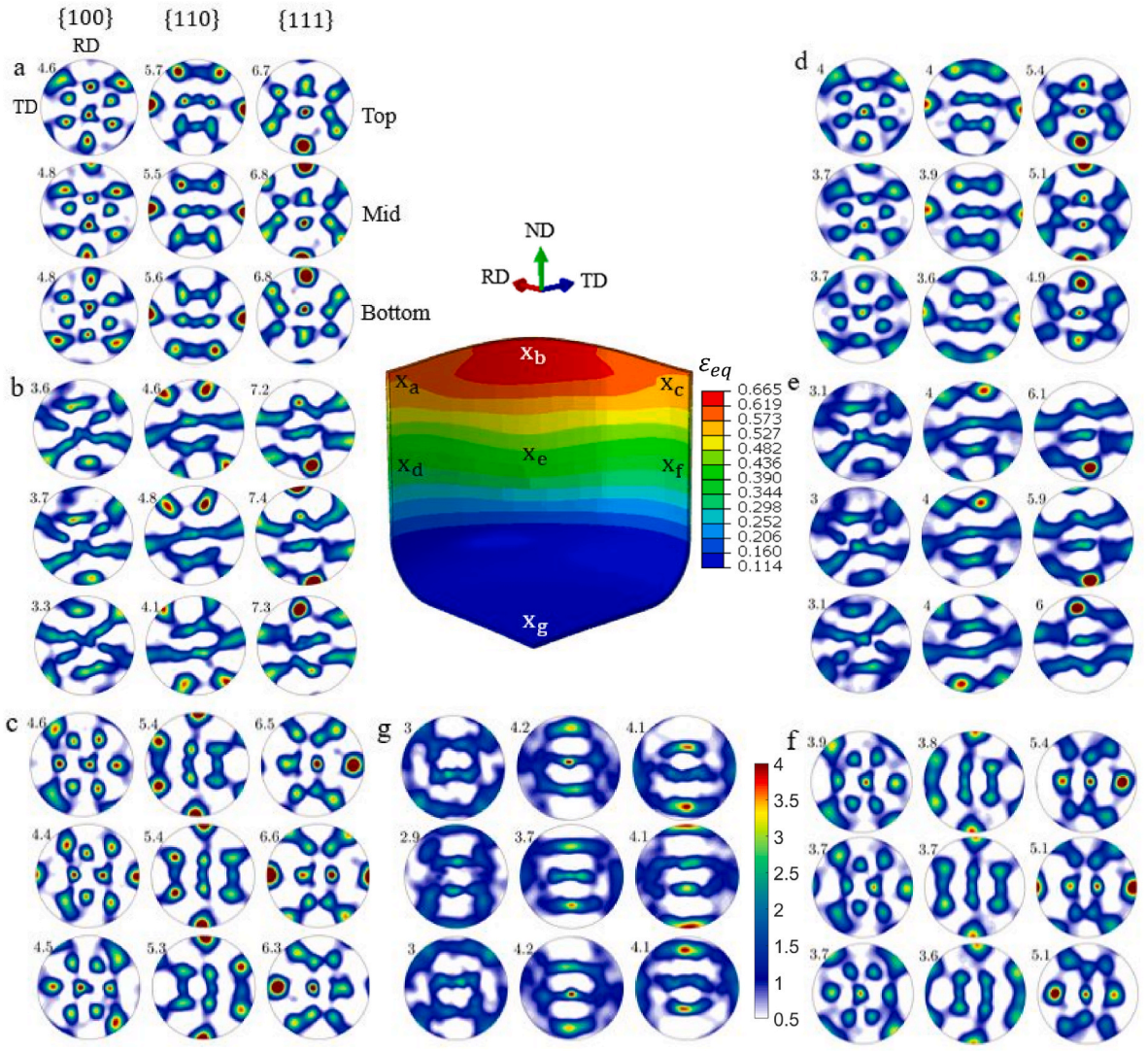

Fig. 19. Equivalent plastic strain contours over the formed cup quarter predicted using FE-FF-VPSC with rolled initial texture surrounded by sets of pole figures showing texture evolution after forming in the through-thickness direction at top, middle and bottom and at several spatial locations (a) rim along RD, (b) rim along 45°, (c) rim along TD, (d) above punch radius along RD, (e) above punch radius along 45°, (f) above punch radius along TD, and (g) at the center. All pole figures are plotted in their global frame where RD is north, and TD is east.

regime and compared with experiments from (Jahedi et al., 2018a).

3.1. *Predicting texture and grain size distributions during HPT of pure Cu*

HPT is a processing technique of metallic specimens subjecting the metal to compression and simultaneous compression and torsion from one end. The technique and benefits have been extensively investigated as means to obtain ultra-fine grain structures (Azzeddine et al., 2022; Horita and Langdon, 2005; Islamgaliev et al., 2001; Jahedi et al., 2015c; Kawasaki et al., 2011; Kim et al., 2003; Zhilyaev and Langdon, 2008). The orientation gradients that develop during such torsional deformation improve the rate of grain refinement (Jahedi et al., 2015a). FE modeling of the processes has been attempted to better understand the mechanical fields including the radial variations of strains (Figueiredo et al., 2011; Jahedi et al., 2014; Yoon et al., 2008). However, the FE modeling was limited to a small number of turns due to convergence issues as the elements of the billet undergo severe distortions (Jahedi et al., 2014, 2015b). A number of studies reported experimental results of grain size evolution during HPT in function of applied pressures and number of turns and other SPD processes (Azzeddine et al., 2022; Jahedi et al., 2017b; Jamalian et al., 2019; Liu et al., 2020; Naghdy et al., 2016) but the modeling works predicting the grain size evolution were limited (Butler and McDowell, 1998; Kumar and Mahesh, 2013; Ostapovets et al., 2012; Toth et al., 2010). The predictions of concomitant evolution of texture and grain size distributions during HPT accomplished in the present work are presented next.

In HPT, the effective shear strain ε_{eq} for a cylindrical/disk specimen can be estimated using (Jahedi et al., 2015b):

$$\varepsilon_{eq} = \frac{2\pi NR}{h\sqrt{3}}, \tag{30}$$

where R is the radial distance from the center of a disk specimen, h is the height/thickness of the sample, and N is the number of turns. Sample height $h = 15$ mm and radius of the disk $R = 5$ mm are taken for the present work from (Jahedi et al., 2017b) to estimate the effective strains of 2.42 and 4.84 for $N = 2$ and 4, respectively using Eq. (30). During HPT process, some slippage occurs between the anvil and specimen which could account for about 20% for 2 turns and increases with the number of turns (Edalati et al., 2009). Assuming 25% slippage, the effective strains become 1.81 and 3.63 for 2 and 4 HPT turns, respectively.

Fig. 1a shows the initial measured texture of an extruded

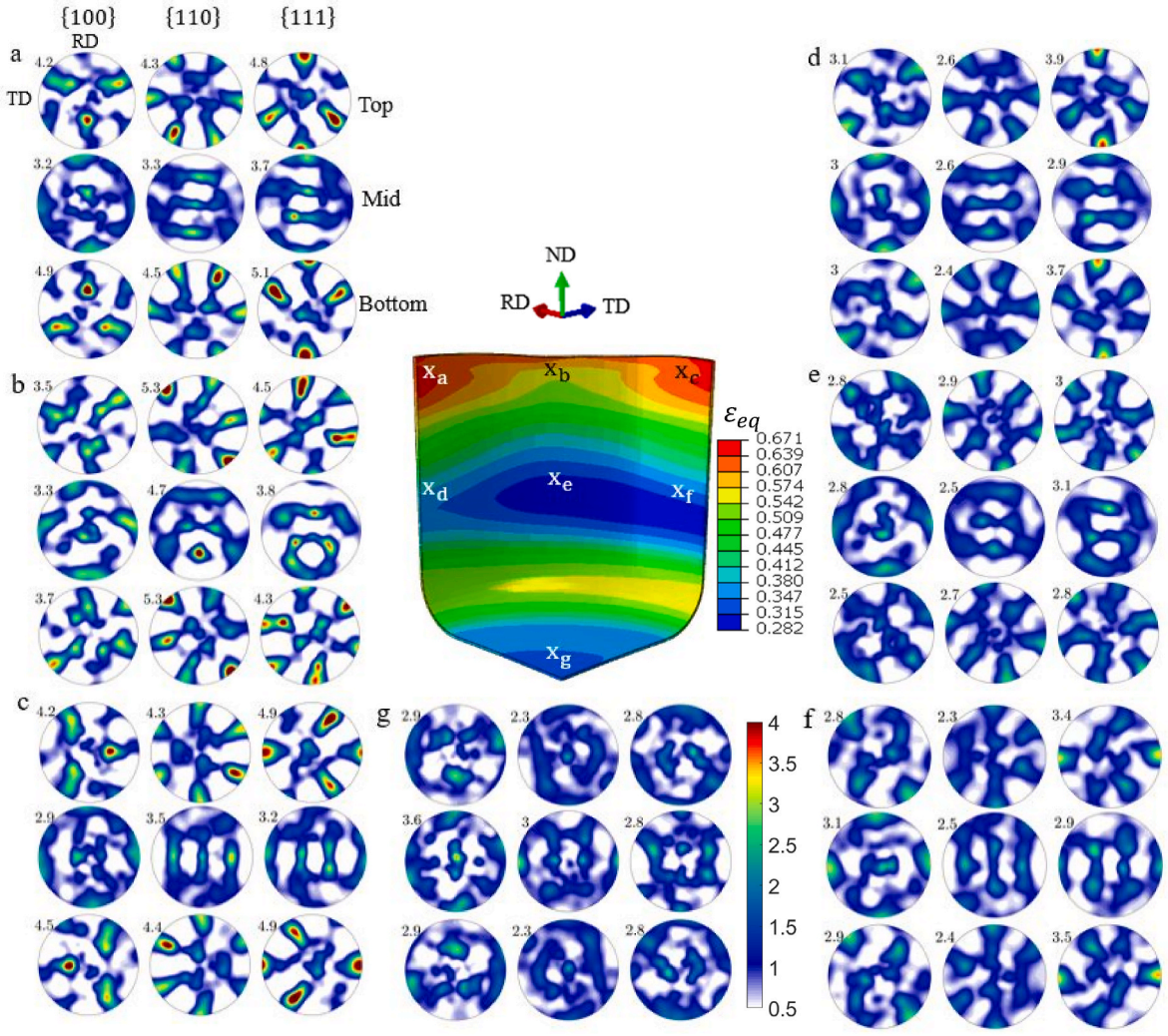

Fig. 20. Equivalent plastic strain contours over the formed cup quarter predicted using FE-FF-VPSC with partially recrystallized initial texture surrounded by sets of pole figures showing texture evolution after forming in the through-thickness direction at top, middle and bottom and at several spatial locations (a) rim along RD, (b) rim along 45°, (c) rim along TD, (d) above punch radius along RD, (e) above punch radius along 45°, (f) above punch radius along TD, and (g) at the center. All pole figures are plotted in their global frame where RD is north, and TD is east.

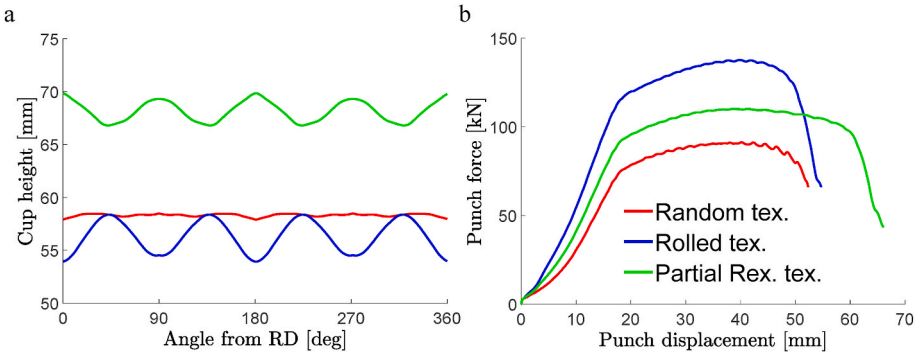

Fig. 21. (a) Cup profile vs. angle from RD and (b) punch force vs. punch displacement using the three types of textures: random, rolled, and partially recrystallized.

commercially pure Cu. The texture used in the simulations was represented using 400 equally weighted orientations. The initial grain diameter, D_i is taken to be 15 μm for all grains. Cu, having face-centered cubic (fcc) crystal structure, was assumed to deforms via $\{111\}\langle 1\bar{1}0\rangle$ slip systems. The dislocation density-based hardening law is used for the evolution of slip resistance. Table 1 shows the dislocation density hardening parameters fitted with the uniaxial experimental compression stress-strain curve. Fig. 2 compared the true stress vs true strain curve in compression along the extrusion direction (ED) for the simulation against the experimental data (Hansen et al., 2013; Jahedi et al., 2015a).

The initial texture and grain size are subjected to simple shear deformation conditions using FF-VPSC. Fig. 1b and c show simulated

deformed textures by simple shear deformation for 2 turns ($\varepsilon_{eq} = 1.81$) and 4 turns ($\varepsilon_{eq} = 3.63$), respectively. These are in good agreement with those experimentally measured as reported in (Jahedi et al., 2017b). The grain size distributions are calculated using Eq. (26) and Eq. (27) after 2 and 4 turns. At a strain level of 1.81 (2 turns), the number of grains (after fragmentation) is 4484, while at 3.63 (4 turns) the number of grains is 9046 from the initial 400. The measured and simulated grain size distributions for 2 and 4 turns are compared in Fig. 3a and b. Evidently, the simulated grain size distributions match reasonably well the measured data. Fig. 4 compares the probability density functions (pdfs) of equivalent isotropic spread (*SD*) for the simulations of 2 and 4 turns (1.81 and 3.63 strain) for all grains. The magnitude of the isotropic spreads increases with the increase of the strain level inducing more fragmentation. Finally, Fig. 5 depicts several discrete representations of the intragranular misorientation spreads in a selected grain with plastic straining. The process of fragmentation can better be appreciated using the figure.

3.2. Predicting texture and grain size distributions after tension and static recrystallization of AA5182-O

For this case study, a 1.55 mm thick sheet specimen of the alloy AA5182-O was pulled in tension along the RD using a continuous bending under tension (CBT) machine to a greater strain level than possible in simple tension (Mayer et al., 2024). Fig. 6 shows inverse pole figure (IPF) maps of the alloy in the as-received state, after CBT to a tensile strain of 0.45, and after full recrystallization (at 280 °C for 2 h). The grain size distributions from the maps are provided in the figure. Finally, pole figures showing texture in the corresponding specimens are provided in Fig. 7. The initial texture is a cube oriented showing evidence of rolling and recrystallization processing of the material. The texture is represented using 400 weighted crystal orientations resembling the initial grain size distribution with the average initial grain size of about 25 μm. The texture after CBT is a relatively strong {111} fiber along the pulling direction, RD. The recrystallized texture is less intense than the deformed one, as expected.

Fig. 8 shows a comparison between measured and simulated stress-strain curves for the alloy in simple tension along the RD direction. The dislocation density-based hardening law parameters are fitted for the alloy and presented in Table 2. The alloy has the fcc crystal structure like Cu and deforms by the same octahedral $\{111\}\langle 1\bar{1}0\rangle$ slip systems like Cu. Furthermore, grain average misorientation (GAM) spreads are obtained from the deformed map for a comparison with model predictions. The normalized distributions of GAM spreads are compared with the corresponding predicted average intragranular misorientation spreads calculated using Eq. (A1) in Fig. 9.

Fig. 10 shows pole figures of predicted deformed texture after tension along RD to a true strain of 0.45. Evidently, the simulated texture evolution is such that the {111} fiber texture peak arises along the pulling direction, RD. Even though the measured and simulated deformation textures show some differences because the CBT process is not exactly simple tension, the predictions are regarded as good. While the texture comparisons are presented in a qualitative way, we have calculated texture difference indices (TDIs) and pole figure differences (PFD) indices between measurements and predictions following the definitions for quantitative texture comparisons presented in (Knezevic and Bhattacharyya, 2017). The indices values of 0 corresponds to a perfect match between measured and predicted pole figures/textures, while the values of 1 corresponds to a perfect mismatch. The obtained values of the indices are <0.1 indicating good quantitative agreement. CBT was a way to successfully pull the alloy to a large strain necessary to promote the appreciable evolution of texture and misorientations (Barrett and Knezevic, 2020; Barrett et al., 2020; Poulin et al., 2019, 2020a, 2020b). The developed deformation texture and misorientation spreads constitute the deformed structure for onset of static recrystallization. Fig. 10 also shows the predicted fully recrystallized texture of the alloy. Table 3 presents the static recrystallization model parameters taken from (Riyad and Knezevic, 2023). The recrystallized texture is not substantially different from the deformed texture but with a lesser intensity than the deformed one. The nucleation type was found to be grain boundary (GB) nucleation, which is also the experimentally observed nucleation mechanism in aluminum alloys after tension (Humphreys and Hatherly, 2004b; Kaibyshev and Malopheyev, 2014; Liu et al., 2003; Lv et al., 2020). Bi-modal grains did not form during tensile deformation and therefore transition bands did not develop. In contrast, the grains developed unimodal spreads favoring the GB nucleation. Therefore, the GB nucleation was favoured. The number of grains after CBT was 603, while the number of grains was 482 after the static recrystallization.

Fig. 11 shows the simulated grain size distribution after the deformation and subsequent static recrystallization compared to the experimental data from Fig. 6c'. Evidently, the agreement is good demonstrating the flexibility of the model to be adjusted for the simulations of grain size distributions.

3.3. Predicting texture and grain size distributions of alloy WE43 undergoing compression in the dynamic recrystallization regime

In the last case, the evolution of texture, grain size, and strength are simulated for the alloy WE43 with hexagonal close-packed (hcp) crystal structure. The initial texture of WE43 was assumed random consisting of 400 equally weighted grains. The alloy was in the as-case condition exhibiting a relatively random texture (Jahedi et al., 2018a). The initial average grain size was taken to be 40 μm, consistent with the experimental measurements. The slip modes available during the deformation of the alloy were prismatic $< \mathbf{a} > \{1\bar{1}00\}\langle 11\bar{2}0\rangle$, basal $< \mathbf{a} > \{0001\}\langle\bar{2}110\rangle$, and first order pyramidal $< \mathbf{c}+\mathbf{a} > \{10\bar{1}1\}\langle 2\bar{1}\bar{1}3\rangle$ (Feather et al., 2019, 2021; Ghorbanpour et al., 2019, 2020; Jahedi et al., 2017c). Twinning was suppressed by the elevated temperature. Texture and grain size distributions were simulated under compression using a strain rate of 0.001 s^{-1} at a temperature of 550 K to a true strain of 1.0. Every deformation increment is followed by a recrystallization increment in the simulation (Zecevic et al., 2020).

Fig. 12 shows the comparison of measured and simulated true stress-strain response. The fitted dislocation density-based hardening law parameters and the recrystallization parameters used in the simulation are the same as those presented in (Zecevic et al., 2020). The dynamic recrystallization in the simulation took place by the GB nucleation. Fig. 13 shows the predicted grain size distribution in the alloy after the thermo-mechanical simulation. After the deformation and dynamic recrystallization, the alloy had 4148 grains with 0.34 vol fraction of the structure recrystallized.

3.4. Rolling, recrystallization, and cup drawing using FE-FF-VPSC

The FE-VPSC UMAT subroutine from (Zecevic et al., 2016a; Zecevic and Knezevic, 2018) has been extended into FE-FF-VPSC to include the field fluctuations terms enabling the grain fragmentation and recrystallization modeling within the commercial FE software Abaqus. A processing sequence involving rolling, recrystallization, and deep drawing of AA6022-T4 is simulated as an application case study for the developed modeling framework. The hardening parameters were fit first to match the stress-strain behavior of the alloy (Zecevic and Knezevic, 2015). The fit is shown in Fig. 14, while the parameters are provided in Table 4.

A rolling model presented in (Zecevic et al., 2015a) is used in the simulation. The setup is shown in Fig. 15a. The half-thickness of the sheet consisted of 396 CPE4 plane strain elements in 2D. The half sheet thickness was modeled by imposing the symmetry boundary conditions due to the orthotropic symmetry. The rolling simulation involved a

single rolling pass having 50% rolling reduction with a friction coefficient of 0.4. The plastic deformation of the half-model was applied via the rotation of the top roll. The roller and the sheet had a hard contact. The rolling simulation was initialized with a 200 equally weighted random crystal orientations. The rolling simulation took about 20 h to complete on a computer workstation using 32 CPUs.

Fig. 15b and c shows the sheet during rolling with strain contours. The rolled textures at the surface and middle of sheet are shown in Fig. 15d. Upon entering the rolls, the sheet near the surface undergoes shearing because of the friction between the contacting surfaces causing heterogeneous deformation. As a result, the metal near the surface experience different deformation history than the metal at the center. These deformation histories determine the evolution of the texture and induce texture gradients across the sheet. The predicted texture at the center of the sheet resembles a typical plane strain conditions fcc texture (Beyerlein et al., 2005), while the predicted texture near the surface resembles the typical simple shear + plain strain conditions fcc texture (Kocks et al., 1998a). Grain fragmentation was active in all integration points during rolling, but recrystallization is only modeled for the two textures, top and center. The fully recrystallized textures at the top and middle of the sheet are shown in Fig. 15e. Fig. 15f shows partially recrystallized textures at the top and middle of the rolled sheet. The nucleation of new grains took place by the transition band nucleation, as necessary to promote cube texture formation (Doherty et al., 1997b). The high stacking fault energy metals like Al, form preferential Cu-type texture during rolling, which is accompanied by a large content of bi-modal grains. Such grains favor the transition band nucleation. The static recrystallization model parameters are provided in Table 5. The partially recrystallized texture underwent 40% recrystallization. The pole figures of both fully and partially recrystallized textures show cube texture features of different intensity especially at the middle of sheet. The predicted recrystallized textures resemble the measured texture of rolled and recrystallized AA6022-T4 alloy presented in (Feng et al., 2020).

The subsequent objective is to use the predicted gradient in texture evolution in the through thickness direction of the sheet as the initial texture in a blank for drawing of a circular cup. Such cup drawing simulation of AA6022-T4 was previously performed in (Feng et al., 2020), but the initial texture in the sheet was a uniform texture throughout the sheet obtained by measurements. The same simulation setup is used here to perform four simulations. The texture gradient after rolling, the two texture gradients after rolling followed by recrystallization, and a random texture were used to initialize the deep drawing of a circular cup simulations. The linked processing sequences consisting of rolling, followed by recrystallization, and finally deep drawing to predict texture evolution from an initially random texture to after deep drawing are simulated for the first time in the present work. As one of the major defects that occurs in the circular cup deep drawing process is known as earing, the performed simulations allowed a study into the effects of initial textures and underlying anisotropy on the formation of earing profiles during deep drawing. Earing is the formation of wavy edges at the open end of the cup with deep drawing. These results are described next.

The four textures are used to initialize the cup drawing simulation as presented in (Feng et al., 2020), one at the time. The simulation setup is given in Fig. 16a. In the depicted quarter setup, the punch is green, die is blue, and die holder is red. The blank undergoing the drawing is in between the die and the die holder. The blank has 14,564C3D8R elements with 4 through-thickness layers. The random texture is assigned uniformly throughout the blank, while the rolled, partial recrystallized, and fully recrystallized textures are initialized with the gradient. The rolled and recrystallized textures are assigned such that the center textures are assigned to elements in the two center layers, while the textures from the surface are assigned as initial textures to the outside element layers of the blank. The integration points of the top elements of the blank (out of the 4 element layers through the thickness) are initialized with top textures, while the integration points of the bottom elements of the blank are initialized with a 180° rotated top textures. The punch and blank are in a soft contact with a coefficient of friction of 0.1. After the cup is drawn, the contact is removed and the springback is simulated in which the stress fields relax accompanied with some geometrical changes. The fields after springback are presented. Each cup drawing simulation took about 100 h to complete on a computer workstation using 32 CPUs.

Fig. 16 shows the FE meshes after forming of the cups for the four initial textures along with a photograph of an experimentally formed cup of the alloy taken from (Tian et al., 2017). Since only a quarter modes were simulated, the predicted quarter cups are mirrored across the 360° range. While the random, rolled, and partially recrystallized textures initialized simulations were successfully completed, the fully recrystallized texture initialized simulation exhibited necking. The drawing was not completed in this case. The fully recrystallized textures can be prone to necking due to the strong cube texture, which appears unfavorable for deep drawing. Similar observation were reported in (Qin et al., 2023) and rationalized via a large planar anisotropy. Fig. 17 shows the equivalent plastic strain contours better revealing the necking region.

Fig. 18 presents the simulated equivalent plastic strain contours over the cup drawn with the random initial texture. Several material points are selected to show the spatial texture evolution over the cup and underlying gradients through the thickness. The top sets of pole figures show the texture evolution at the surface of the cup, the middle sets of pole figures show the texture evolution in the center regions, and the bottom sets of pole figures show the texture evolution at the other surface of the cup at each location. The pole figures are plotted in global frame where RD is north, and TD is east. Evidently, the texture gradient through the thickness is not that pronounced for the random initial texture, while spatially there are some differences in the texture formation during the drawing. Figs. 19 and 20 present the same simulation results for the cup drawing simulations initialized with the rolled and partially recrystallized textures, respectively. The texture gradients are evident in these cases along with the spatial variations of the predicted texture evolution. The pole figures at the bottom of the cups (the location g) do not show substantial texture evolution. The cup is the most severely deformed around the top at locations a, b, and c, where the cup experiences shear and circumferential compression. The deformation textures are the sharpest at these locations. The pole figures at locations d, e, and f are similar but weaker than those at the locations a, b, and c owing to less plastic strain. The gradient in textures remained during the cup drawing processes.

Fig. 21a compares the simulated cup profiles vs. angle from the RD after springback for the three types of initial textures. The simulated earing profile induced by the random initial texture is small. The rolled texture induces the largest earing profile owing to the largest texture intensity. The partially recrystallized texture profile resembles closely the measure profile as seen in Fig. 16 because a partially recrystallized texture is present in the alloy used in the experiment. With the partially recrystallized gradient texture, the cup height peaks at 0° and 90° from the RD, which matches well the measurements presented in (Feng et al., 2020; Tian et al., 2017). Fig. 21b shows the simulated punch force vs. punch displacement using the three types of textures. Slip resistance was initial for all grains of the random initial texture. Therefore, the required force is the lowest. The simulation using the partially recrystallized texture required a larger force compared to the random texture because slip resistances within unrecrystallized grains were carried over from the rolling process, while those in recrystallized grains were initialized. Also, the displacement was the greatest for the partially recrystallized texture. As a result, the cup height is the greatest along with the significant reduction in thickness of cup. Finally, the punch force was the greatest for the rolled texture because the slip resistances in grains were carried over from the prior rolling simulation for all grains.

4. Conclusions

This paper advanced the field fluctuations viscoplastic self-consistent (FF-VPSC) crystal plasticity model to predict not only the evolution of texture in polycrystalline metals undergoing deformation and recrystallization but also the evolution of grain size distributions. The key aspect of the model is the consideration of the intragranular misorientation spreads, which enabled the grain fragmentation and recrystallization models within FF-VPSC. The FF-VPSC model is also physically-based because it incorporates a dislocation density-based hardening law for the evolution of slip system resistance. The FF-VPSC model is further coupled with the implicit FEM framework into a FE-FF-VPSC user material subroutine in Abaqus to facilitate predicting geometrical shape changes under complex boundary conditions.

The FF-VPSC model incorporating the grain fragmentation and recrystallization models was validated by predicting the evolution of texture, grain size, and misorientation spreads under high pressure tension of Cu, tension of AA5182-O, and compression in the dynamic recrystallization regime of WE43. These predictions during both deformation and recrystallization were found to be in good agreement with the corresponding measurements. The FE-FF-VPSC model was applied to predict texture gradients forming during rolling and subsequent recrystallization of AA6022-T4. The signature cube texture developing during partial or full recrystallization of the alloy was successfully predicted. The predicted gradient in texture after rolling and recrystallization were used along with a reference random texture to initialize cup drawing simulations using FE-FF-VPSC. The simulated processing sequences of rolling, recrystallization, and deep-drawing of a circular cups demonstrated the versatility of the developed FE-FF-VPSC simulation framework in predicting texture evolution and phenomena pertaining to the behavior of materials and also geometrical share changes important for the optimization of metal forming processes. To this end, the effects of initial texture and underlying anisotropy on the formation of earing profiles during deep drawing were simulated. The blank initialized with a partially recrystallized initial texture was formed into a cup with earing profile which resembled closely the measured earing profile.

Future work will focus on advancing the FF-VPSC into a strain gradient SG-VPSC formulation capable of calculating the geometrically necessary dislocations from the misorientation spreads to improve hardening and underlying backstress fields influencing slip system activation in an even more physical sense within a future FE-SG-VPSC model. Moreover, the recrystallization modeling performed in the present work was grain size insensitive. It is known that grain size influences the rate of recrystallization and therefore the rate of formation of shear or transition bands e.g. (Zhang et al., 2017). Future works will consider implementing the improvements pertaining to the grain size sensitive recrystallization kinetics within the size sensitive framework of FE-SG-VPSC as appropriate data sets become available for the model calibration and comparisons.

CRediT authorship contribution statement

Iftekhar A. Riyad: Writing – original draft, Visualization, Validation, Investigation, Formal analysis. **Marko Knezevic:** Writing – review & editing, Supervision, Software, Resources, Project administration, Methodology, Investigation, Funding acquisition, Conceptualization.

Declaration of competing interest

The authors declare that they have no known competing financial interests or personal relationships that could have appeared to influence the work reported in this paper.

Acknowledgements

This research was based upon a project supported by the U.S. National Science Foundation under a DMREF grant CMMI-2118557.

Appendix A

Recrystallization model

Nucleation and growth of new grains during recrystallization is driven by the deformed microstructure (Doherty et al., 1997a; Humphreys and Hatherly, 2004a; Tam et al., 2021). Experiments have shown that spatial orientation gradients and strain energy distributions drive recrystallization. In particular, transition bands and grain boundaries act as the locations for grain nucleation (Humphreys and Hatherly, 2004b). The recrystallization model described in (Zecevic et al., 2019, 2020) is used in the present work, as briefly summarized below.

The thresholds, *th*, for strain energy, E_{th}^{gb} and E_{th}^{tb}, and the thresholds for average misorientation angle of local neighboring orientations, $\delta\theta_{th}^{gb}$ and $\delta\theta_{th}^{tb}$, in each grain must be satisfied first for the process of recrystallization to start for either grain boundary, *gb*, or transition bands, *tb*, nucleation mechanisms. The average misorientation angle between the local neighborhood points inside a grain is defined as (Riyad and Knezevic, 2023; Zecevic et al., 2019):

$$\langle \delta\theta \rangle^{(r)} \approx 2\sqrt{2\mathbf{I} : \langle \delta\mathbf{r} \otimes \delta\mathbf{r} \rangle^{(r)}}. \tag{A1}$$

The strain energy in a grain is given by (Hirth and Lothe, 1982; Hull and Bacon, 2001; Wenk et al., 1997):

$$E^{(r)} = \rho^{(r)} \mu b^2 / 2, \tag{A2}$$

where $\rho^{(r)}$ is the dislocation density, b is the Burgers vector, and μ is the shear modulus. A dislocation density-based hardening law is used in the present work to explicitly model the dislocation density per grain.

In our model, the nucleation can occur at grain boundaries or in transition bands, while grain growth is driven by the difference in stored energy between a given grain and HEM (Engler, 1996; Humphreys and Hatherly, 2004a). After the thresholds are satisfied, the probabilities of grain boundary and transition band nucleation, $P_{gb}^{(r)}$ and $P_{tb}^{(r)}$, for a grain of weight $w^{(r)}$ and area, A in time Δt are as follows:

$$P_{gb}^{(r)}(\Delta t, w^{(r)}, E^{(r)}) = 1 - \left(1 - B_{gb} \exp\left(-\frac{A_{gb}}{E^{(r)2}}\right)\right)^{\frac{dt}{\Delta t}\left(\frac{w^{(r)}}{dw}\right)^{2/3}}, \tag{A3}$$

$$P_{tb}^{(r)}(\Delta t, w^{(r)}, E^{(r)}) = 1 - \left(1 - B_{tb} \exp\left(-\frac{A_{tb}}{E^{(r)2}}\right)\right)^{\frac{dt}{\Delta t}\left(\frac{w^{(r)}}{dw}\right)^{2/3}}, \tag{A4}$$

where the grain with an area A is subdivided into large number of small areas dA having weight dw. B_{gb} and B_{tb} are pre-exponential factors scaling the probability, while A_{gb} or A_{tb} are additional fitting parameters that determine likelihood of nucleation along with the strain energy. After calculating these nucleation probabilities, they are compared to a random number between 0 and 1. If any probability is greater than the random number, a new grain nucleates having a weight of $w_{nuc} = 0.0001$. The newly nucleated grain has a zero-strain energy and an initial value of slip resistance taken from the deformation model.

Growth of a nucleated grain takes place by the mobility and velocity of its grain boundary via the following relation:

$$v^{(r)} = M(E^{avg} - E^{(r)}), \tag{A5}$$

where M is the mobility of the boundary as a fitting parameter, $v^{(r)}$ is the boundary velocity of each grain, $E^{(r)}$ is the stored energy of the grain, and $E^{avg} = \sum_r w^{(r)} E^{(r)}$ is the stored energy of HEM. The mobility rate can be fit to achieve a balance between nucleation of recrystallized grains and growth. A lower mobility rate results in a larger number of recrystallized grains and vice versa. Nevertheless, other parameters such as Δt and the mechanism of nucleation also influence the number of recrystallized grains i.e. the resulting grain size.

Finally, the change of weight of the grain due to its boundary migration with velocity $v^{(r)}$ from time t to $t + \Delta t$ is given by (Wenk et al., 1997):

$$w^{(r),t+\Delta t} = w^{(r),t} + 3M\left(\frac{4\pi}{3}\right)^{\frac{1}{3}} (w^{(r),t})^{\frac{2}{3}} (E^{avg} - E^{(r)})\Delta t. \tag{A6}$$

The volume of fully recrystallized grains must remain the same as the volume of the original grains. If this happens then the full recrystallization is achieved because any remaining weights of unrecrystallized grains got exhausted. Otherwise, the process is a partial recrystallization.

Hardening law

A brief summary of the dislocation density hardening law (Beyerlein and Tomé, 2008; Knezevic et al., 2015; Proust et al., 2007; Zecevic and Knezevic, 2018; Zecevic et al., 2016b) used in FF-VPSC is presented next. The slip resistance per slip system s, τ_c^s, is given by:

$$\tau_c^s = \tau_0^\alpha + \tau_{for}^s + \tau_{sub}^\alpha, \tag{A7}$$

where τ_0^α is the initial nonevolving slip resistance per slip mode, α; τ_{for}^s and τ_{sub}^α are evolving slip resistance terms due to accumulation of forest dislocations, ρ_{for}^s and substructure/debris dislocations, ρ_{sub} respectively. The contribution to the resistance to slip due to forest dislocations, τ_{for}^s is given as:

$$\tau_{for}^s = \chi b^\alpha \mu^\alpha \sqrt{\rho_{for}^s}, \tag{A8}$$

where χ is the dislocation interaction constant set to 0.9, b^α is the magnitude of Burgers vector, and μ^α is the shear modulus. The contribution to the resistance to slip due to substructure dislocations is given as:

$$\tau_{sub}^\alpha = 0.086\mu^\alpha b^\alpha \sqrt{\rho_{sub}} \log\left(\frac{1}{b^\alpha \sqrt{\rho_{sub}}}\right). \tag{A9}$$

The evolution of forest dislocation density, ρ_{for}^s is driven by the balance between the rate of dislocation generation and recovery or removal and can be expressed as (Mecking and Kocks, 1981):

$$\frac{\partial \rho_{for}^s}{\partial \gamma^s} = \frac{\partial \rho_{gen,for}^s}{\partial \gamma^s} - \frac{\partial \rho_{rem,for}^s}{\partial \gamma^s} = k_1^s \sqrt{\rho_{for}^s} - k_2^s(\dot{\varepsilon}, T)\rho_{for}^s, \tag{A10}$$

where k_1^s is one fitting parameter for dislocation storage due to statistical trapping of mobile dislocations, while k_2^s is another coefficient which accounts for dislocation recovery/removal by thermally activated mechanisms. The latter is strain rate sensitive and is expressed as:

$$k_2^s = \frac{k_1^s}{\sqrt{\sum_{s'} (\chi^{-1})^{ss'} \left(\frac{\tau_{sat}^{s'}}{b^{s'}\mu^{s'}}\right)^2}}, \tag{A11}$$

where

$$\tau_{sat}^s = \frac{D^\alpha (b^\alpha)^3 g^\alpha \mu^\alpha}{D^\alpha (b^\alpha)^3 - kT \log\left(\frac{\dot{\varepsilon}}{\dot{\varepsilon}_0}\right)}, \tag{A12}$$

where k is the Boltzmann constant, $\dot{\varepsilon}_0 = 10^7 s^{-1}$ is the reference strain rate, g^α is the activation enthalpy, D^α is the drag stress, and T is the temperature. Finally, the substructure/debris dislocation density forms due to a fraction of removed forest dislocations and can be expressed as:

$$\Delta\rho_{sub} = q^{\alpha} b^{\alpha} \sqrt{\rho_{sub}} \frac{\partial \rho^{s}_{rem,for}}{\partial \gamma^{s}} |d\gamma^{s}|. \tag{A13}$$

where q^{α} is a fitting rate coefficient that determines a fraction of dislocations that form substructure, while the remaining fraction annihilates.

Data availability

Data will be made available on request.

References

Asaro, R.J., 1979. Geometrical effects in the inhomogeneous deformation of ductile single crystals. Acta Metall. 27, 445–453.

Asaro, R.J., Needleman, A., 1985. Texture development and strain hardening in rate dependent polycrystals. Acta Metall. Mater. 33, 923–953.

Asaro, R.J., Rice, J.R., 1977. Strain localization in ductile single crystals. J. Mech. Phys. Solid. 25, 309–338.

Azushima, A., Kopp, R., Korhonen, A., Yang, D.Y., Micari, F., Lahoti, G.D., Groche, P., Yanagimoto, J., Tsuji, N., Rosochowski, A., Yanagida, A., 2008. Severe plastic deformation (SPD) processes for metals. CIRP Annals 57, 716–735.

Azzeddine, H., Bradai, D., Baudin, T., Langdon, T.G., 2022. Texture evolution in high-pressure torsion processing. Prog. Mater. Sci. 125, 100886.

Barrett, T.J., Knezevic, M., 2020. Modeling material behavior during continuous bending under tension for inferring the post-necking strain hardening response of ductile sheet metals: application to DP 780 steel. Int. J. Mech. Sci. 174, 105508.

Barrett, T.J., Takagi, S., Islam, N., Kuwabara, T., Hassan, T., Kinsey, B.L., Knezevic, M., Korkolis, Y.P., 2020. Material modeling and simulation of continuous-bending-under-tension of AA6022-T4. J. Mater. Process. Technol., 116658

Beyerlein, I., Li, S., Necker, C., Alexander, D., Tomé, C., 2005. Non-uniform microstructure and texture evolution during equal channel angular extrusion. Phil. Mag. 85, 1359–1394.

Beyerlein, I.J., Lebensohn, R.A., Tomé, C.N., 2003. Modeling texture and microstructural evolution in the equal channel angular extrusion process. Mater. Sci. Eng., A 345, 122–138.

Beyerlein, I.J., Tomé, C.N., 2008. A dislocation-based constitutive law for pure Zr including temperature effects. Int. J. Plast. 24, 867–895.

Beyerlein, I.J., Tóth, L.S., 2009. Texture evolution in equal-channel angular extrusion. Prog. Mater. Sci. 54, 427–510.

Butler, G.C., McDowell, D.L., 1998. Polycrystal constraint and grain subdivision. Int. J. Plast. 14, 703–717.

Das, S., Ponte Castañeda, P., 2021. Statistics of the stress, strain-rate and spin fields in viscoplastic polycrystals. Int. J. Solid Struct. 217–218, 193–214.

Dillamore, I., Katoh, H., 1974. Mechanisms of recrystallization in cubic metals with particular reference to their orientation-dependence. Met. Sci. 8, 73–83.

Doherty, R., Hughes, D., Humphreys, F., Jonas, J., Jensen, D.J., Kassner, M., King, W., McNelley, T., McQueen, H., Rollett, A., 1997a. Current issues in recrystallization: a review. Mater. Sci. Eng., A 238, 219–274.

Doherty, R., Hughes, D., Humphreys, F., Jonas, J.J., Jensen, D.J., Kassner, M., King, W., McNelley, T., McQueen, H., Rollett, A., 1997b. Current issues in recrystallization: a review. Mater. Sci. Eng., A 238, 219–274.

Edalati, K., Horita, Z., Langdon, T.G., 2009. The significance of slippage in processing by high-pressure torsion. Scripta Mater. 60, 9–12.

Eghtesad, A., Germaschewski, K., Knezevic, M., 2022. Coupling of a multi-GPU accelerated elasto-visco-plastic fast Fourier transform constitutive model with the implicit finite element method. Comput. Mater. Sci. 208, 111348.

Eghtesad, A., Germaschewski, K., Lebensohn, R.A., Knezevic, M., 2020. A multi-GPU implementation of a full-field crystal plasticity solver for efficient modeling of high-resolution microstructures. Comput. Phys. Commun. 107231.

Eghtesad, A., Knezevic, M., 2020. High-performance full-field crystal plasticity with dislocation-based hardening and slip system back-stress laws: application to modeling deformation of dual-phase steels. J. Mech. Phys. Solid. 134, 103750.

Eghtesad, A., Knezevic, M., 2021. A full-field crystal plasticity model including the effects of precipitates: application to monotonic, load reversal, and low-cycle fatigue behavior of Inconel 718. Mater. Sci. Eng., A 803, 140478.

Engler, O., 1996. Nucleation and growth during recrystallisation of aluminium alloys investigated by local texture analysis. Mater. Sci. Technol. 12, 859–872.

Eshelby, J.D., Peierls, R.E., 1997. The determination of the elastic field of an ellipsoidal inclusion, and related problems. Proc. Roy. Soc. Lond. A Math. Phys. Sci. 241, 376–396.

Feather, W.G., Ghorbanpour, S., Savage, D.J., Ardeljan, M., Jahedi, M., McWilliams, B.A., Gupta, N., Xiang, C., Vogel, S.C., Knezevic, M., 2019. Mechanical response, twinning, and texture evolution of WE43 magnesium-rare earth alloy as a function of strain rate: experiments and multi-level crystal plasticity modeling. Int. J. Plast. 120, 180–204.

Feather, W.G., Lim, H., Knezevic, M., 2020. A numerical study into element type and mesh resolution for crystal plasticity finite element modeling of explicit grain structures. Comput. Mech.

Feather, W.G., Savage, D.J., Knezevic, M., 2021. A crystal plasticity finite element model embedding strain-rate sensitivities inherent to deformation mechanisms: application to alloy AZ31. Int. J. Plast. 143, 103031.

Feng, Z., Yoon, S.-Y., Choi, J.-H., Barrett, T.J., Zecevic, M., Barlat, F., Knezevic, M., 2020. A comparative study between elasto-plastic self-consistent crystal plasticity and anisotropic yield function with distortional hardening formulations for sheet metal forming. Mech. Mater. 148, 103422.

Figueiredo, R.B., Cetlin, P.R., Langdon, T.G., 2011. Using finite element modeling to examine the flow processes in quasi-constrained high-pressure torsion. Mater. Sci. Eng., A 528, 8198–8204.

Ghorbanpour, S., McWilliams, B.A., Knezevic, M., 2019. Low-cycle fatigue behavior of rolled WE43-T5 magnesium alloy. Fatig. Fract. Eng. Mater. Struct. 42, 1357–1372.

Ghorbanpour, S., McWilliams, B.A., Knezevic, M., 2020. Effects of environmental temperature and sample pre-straining on high cycle fatigue strength of WE43-T5 magnesium alloy. Int. J. Fatigue 141, 105903.

Hall, E.O., 1951. The deformation and ageing of mild steel: III discussion of results. Proc. Phys. Soc. 643, 747–752.

Hansen, B.L., Carpenter, J.S., Sintay, S.D., Bronkhorst, C.A., McCabe, R.J., Mayeur, J.R., Mourad, H.M., Beyerlein, I.J., Mara, N.A., Chen, S.R., Gray, G.T., 2013. Modeling the texture evolution of Cu/Nb layered composites during rolling. Int. J. Plast. 49, 71–84.

Hansen, N., 2004. Hall–Petch relation and boundary strengthening. Scripta Mater. 51, 801–806.

Hill, 1966. Generalized constitutive relations for incremental deformation of metal crystals by multislip. J. Mech. Phys.Solids 14, 95–102.

Hill, R., Rice, J.R., 1972. Constitutive analysis of elastic-plastic crystals at arbitrary strain. J. Mech. Phys. Solid. 20, 401–413.

Hirth, J.P., Lothe, J., 1982. Theory of dislocations.

Horita, Z., Langdon, T.G., 2005. Microstructures and microhardness of an aluminum alloy and pure copper after processing by high-pressure torsion. Mater. Sci. Eng., A 410–411, 422–425.

Hull, D., Bacon, D.J., 2001. Introduction to Dislocations. Butterworth-Heinemann.

Humphreys, F., Hatherly, M., 2004a. Recrystallization and Related Annealing Phenomena, 2004. Elsevier.

Humphreys, F.J., Hatherly, M., 2004b. Chapter 7 - recrystallization of single-phase alloys. In: Humphreys, F.J., Hatherly, M. (Eds.), Recrystallization and Related Annealing Phenomena, second ed. Elsevier, Oxford, pp. 215–IV.

Islamgaliev, R.K., Buchgraber, W., Kolobov, Y.R., Amirkhanov, N.M., Sergueeva, A.V., Ivanov, K.V., Grabovetskaya, G.P., 2001. Deformation behavior of Cu-based nanocomposite processed by severe plastic deformation. Mater. Sci. Eng., A 319–321, 872–876.

Jahedi, M., Ardeljan, M., Beyerlein, I.J., Paydar, M.H., Knezevic, M., 2015a. Enhancement of orientation gradients during simple shear deformation by application of simple compression. J. Appl. Phys. 117, 214309.

Jahedi, M., Ardjmand, E., Knezevic, M., 2017a. Microstructure metrics for quantitative assessment of particle size and dispersion: application to metal-matrix composites. Powder Technol. 311, 226–238.

Jahedi, M., Beyerlein, I.J., Paydar, M.H., Zheng, S., Xiong, T., Knezevic, M., 2017b. Effects of pressure and number of turns on microstructural homogeneity developed in high-pressure double torsion. Metall. Mater. Trans. A 48, 1249–1263.

Jahedi, M., Knezevic, M., Paydar, M., 2015b. High-pressure double torsion as a severe plastic deformation process: experimental procedure and finite element modeling. J. Mater. Eng. Perform. 24, 1471–1482.

Jahedi, M., McWilliams, B.A., Kellogg, F.R., Beyerlein, I.J., Knezevic, M., 2018a. Rate and temperature dependent deformation behavior of as-cast WE43 magnesium-rare earth alloy manufactured by direct-chill casting. Mater. Sci. Eng., A 712, 50–64.

Jahedi, M., McWilliams, B.A., Knezevic, M., 2018b. Deformation and fracture mechanisms in WE43 magnesium-rare earth alloy fabricated by direct-chill casting and rolling. Mater. Sci. Eng., A 726, 194–207.

Jahedi, M., McWilliams, B.A., Moy, P., Knezevic, M., 2017c. Deformation twinning in rolled WE43-T5 rare earth magnesium alloy: influence on strain hardening and texture evolution. Acta Mater. 131, 221–232.

Jahedi, M., Paydar, M.H., Knezevic, M., 2015c. Enhanced microstructural homogeneity in metal-matrix composites developed under high-pressure-double-torsion. Mater. Char. 104, 92–100.

Jahedi, M., Paydar, M.H., Zheng, S., Beyerlein, I.J., Knezevic, M., 2014. Texture evolution and enhanced grain refinement under high-pressure-double-torsion. Mater. Sci. Eng., A 611, 29–36.

Jamalian, M., Hamid, M., De Vincentis, N., Buck, Q., Field, D.P., Zbib, H.M., 2019. Creation of heterogeneous microstructures in copper using high-pressure torsion to enhance mechanical properties. Mater. Sci. Eng., A 756, 142–148.

Kaibyshev, R., Malopheyev, S., 2014. Mechanisms of dynamic recrystallization in aluminum alloys. Mater. Sci. Forum 794–796, 784–789.

Kalidindi, S.R., Knezevic, M., Niezgoda, S., Shaffer, J., 2009. Representation of the orientation distribution function and computation of first-order elastic properties closures using discrete Fourier transforms. Acta Mater. 57, 3916–3923.

Kawasaki, M., Figueiredo, R.B., Langdon, T.G., 2011. An investigation of hardness homogeneity throughout disks processed by high-pressure torsion. Acta Mater. 59, 308–316.

Kim, H.S., Hong, S.I., Lee, Y.S., Dubravina, A.A., Alexandrov, I.V., 2003. Deformation behavior of copper during a high pressure torsion process. J. Mater. Process. Technol. 142, 334–337.

Knezevic, M., Beyerlein, I.J., 2018. Multiscale modeling of microstructure-property relationships of polycrystalline metals during thermo-mechanical deformation. Adv. Eng. Mater. 20, 1700956.
Knezevic, M., Bhattacharyya, A., 2017. Characterization of microstructure in Nb rods processed by rolling: Effect of grooved rolling die geometry on texture uniformity. Int. J. Refract. Metals Hard Mater. 66, 44–51.
Knezevic, M., Crapps, J., Beyerlein, I.J., Coughlin, D.R., Clarke, K.D., McCabe, R.J., 2016a. Anisotropic modeling of structural components using embedded crystal plasticity constructive laws within finite elements. Int. J. Mech. Sci. 105, 227–238.
Knezevic, M., Drach, B., Ardeljan, M., Beyerlein, I.J., 2014a. Three dimensional predictions of grain scale plasticity and grain boundaries using crystal plasticity finite element models. Comput. Methods Appl. Mech. Eng. 277, 239–259.
Knezevic, M., Jahedi, M., Korkolis, Y.P., Beyerlein, I.J., 2014b. Material-based design of the extrusion of bimetallic tubes. Comput. Mater. Sci. 95, 63–73.
Knezevic, M., McCabe, R.J., Lebensohn, R.A., Tomé, C.N., Liu, C., Lovato, M.L., Mihaila, B., 2013. Integration of self-consistent polycrystal plasticity with dislocation density based hardening laws within an implicit finite element framework: application to low-symmetry metals. J. Mech. Phys. Solid. 61, 2034–2046.
Knezevic, M., Poulin, C.M., Zheng, X., Zheng, S., Beyerlein, I.J., 2019. Strengthening of alloy AA6022-T4 by continuous bending under tension. Mater. Sci. Eng., A 758, 47–55.
Knezevic, M., Zecevic, M., Beyerlein, I.J., Bingert, J.F., McCabe, R.J., 2015. Strain rate and temperature effects on the selection of primary and secondary slip and twinning systems in HCP Zr. Acta Mater. 88, 55–73.
Knezevic, M., Zecevic, M., Beyerlein, I.J., Lebensohn, R.A., 2016b. A numerical procedure enabling accurate descriptions of strain rate-sensitive flow of polycrystals within crystal visco-plasticity theory. Comput. Methods Appl. Mech. Eng. 308, 468–482.
Kocks, U.F., Tome, C.N., Wenk, H.-R., 1998a. Texture and Anisotropy. Cambridge University Press, Cambridge.
Kocks, U.F., Tomé, C.N., Wenk, H.-R., 1998b. Texture and Anisotropy. Cambridge University Press, Cambridge, UK.
Kumar, M.A., Mahesh, S., 2013. Subdivision and microtexture development in fcc grains during plane strain compression. Int. J. Plast. 44, 95–110.
Lebensohn, R.A., Brenner, R., Castelnau, O., Rollett, A.D., 2008. Orientation image-based micromechanical modelling of subgrain texture evolution in polycrystalline copper. Acta Mater. 56, 3914–3926.
Lebensohn, R.A., Kanjarla, A.K., Eisenlohr, P., 2012. An elasto-viscoplastic formulation based on fast Fourier transforms for the prediction of micromechanical fields in polycrystalline materials. Int. J. Plast. 32–33, 59–69.
Lebensohn, R.A., Tomé, C.N., 1993. A self-consistent anisotropic approach for the simulation of plastic deformation and texture development of polycrystals: application to zirconium alloys. Acta Metall. Mater. 41, 2611–2624.
Lebensohn, R.A., Tomé, C.N., Castaneda, P.P., 2007. Self-consistent modelling of the mechanical behaviour of viscoplastic polycrystals incorporating intragranular field fluctuations. Phil. Mag. 87, 4287–4322.
Lebensohn, R.A., Zecevic, M., Knezevic, M., McCabe, R.J., 2016. Average intragranular misorientation trends in polycrystalline materials predicted by a viscoplastic self-consistent approach. Acta Mater. 104, 228–236.
Liu, W.C., Zhai, T., Morris, J.G., 2003. Comparison of recrystallization and recrystallization textures in cold-rolled DC and CC AA 5182 aluminum alloys. Mater. Sci. Eng., A 358, 84–93.
Liu, Y., Lu, C., Wang, H., Tieu, A.K., Liu, B., 2020. Microstructure evolution, lattice rotation retardation and grain orientation fragmentation in commercial purity aluminium deformed by high pressure torsion. J. Mater. Res. Technol. 9, 6642–6654.
Liu, Y., Ponte Castañeda, P., 2004. Second-order theory for the effective behavior and field fluctuations in viscoplastic polycrystals. J. Mech. Phys. Solid. 52, 467–495.
Lv, J., Zheng, J.-H., Yardley, V.A., Shi, Z., Lin, J., 2020. A review of microstructural evolution and modelling of aluminium alloys under hot forming conditions. Metals 10, 1516.
Masson, R., Bornert, M., Suquet, P., Zaoui, A., 2000. An affine formulation for the prediction of the effective properties of nonlinear composites and polycrystals. J. Mech. Phys. Solid. 48, 1203–1227.
Mayer, S., Matukhno, N., Kinsey, B.L., Knezevic, M., Ha, J., 2024. Manipulation of strength and ductility of AA5182-O through cyclic bending under tension and annealing processing. J. Manuf. Process. 124, 673–688.
Mecking, H., Kocks, U.F., 1981. Kinetics of flow and strain-hardening. Acta Metall. Mater. 29, 1865–1875.
Mercier, S., Molinari, A., 2009. Homogenization of elastic–viscoplastic heterogeneous materials: self-consistent and Mori-Tanaka schemes. Int. J. Plast. 25, 1024–1048.
Meyers, M.A., Chawla, K.K., 2008. Mechanical Behavior of Materials. Cambridge university press.
Miller, A.C., Rice, T.R., 1983. Discrete approximations of probability distributions. Manag. Sci. 29, 352–362.
Molinari, A., Canova, G.R., Ahzi, S., 1987. A self consistent approach of the large deformation polycrystal viscoplasticity. Acta Metall. 35, 2983–2994.
Naghdy, S., Kestens, L., Hertelé, S., Verleysen, P., 2016. Evolution of microstructure and texture in commercial pure aluminum subjected to high pressure torsion processing. Mater. Char. 120, 285–294.
Nagra, J.S., Brahme, A., Lévesque, J., Mishra, R., Lebensohn, R.A., Inal, K., 2020. A new micromechanics based full field numerical framework to simulate the effects of dynamic recrystallization on the formability of HCP metals. Int. J. Plast. 125, 210–234.
Ostapovets, A., Šedá, P., Jäger, A., Lejček, P., 2012. New misorientation scheme for a visco-plastic self-consistent model: equal channel angular pressing of magnesium single crystals. Int. J. Plast. 29, 1–12.
Peirce, D., Asaro, R.J., Needleman, A., 1982. An analysis of nonuniform and localized deformation in ductile single crystals. Acta Metall. 30, 1087–1119.
Petch, N.J., 1953. The cleavage strength of polycrystals. J. Iron Steel Inst. Lond. 173, 25–28.
Ponte Castañeda, P., 2002a. Second-order homogenization estimates for nonlinear composites incorporating field fluctuations: I—theory. J. Mech. Phys. Solid. 50, 737–757.
Ponte Castañeda, P., 2002b. Second-order homogenization estimates for nonlinear composites incorporating field fluctuations: II—applications. J. Mech. Phys. Solid. 50, 759–782.
Popova, E., Brahme, A.P., Staraselski, Y., Agnew, S.R., Mishra, R.K., Inal, K., 2016. Effect of extension 101-2 twins on texture evolution at elevated temperature deformation accompanied by dynamic recrystallization. Mater. Des. 96, 446–457.
Popova, E., Staraselski, Y., Brahme, A., Mishra, R.K., Inal, K., 2015. Coupled crystal plasticity – probabilistic cellular automata approach to model dynamic recrystallization in magnesium alloys. Int. J. Plast. 66, 85–102.
Poulin, C.M., Barrett, T.J., Knezevic, M., 2020a. Inferring post-necking strain hardening behavior of sheets by a combination of continuous bending under tension testing and finite element modeling. Exp. Mech. 60, 459–473.
Poulin, C.M., Korkolis, Y.P., Kinsey, B.L., Knezevic, M., 2019. Over five-times improved elongation-to-fracture of dual-phase 1180 steel by continuous-bending-under-tension. Mater. Des. 161, 95–105.
Poulin, C.M., Vogel, S.C., Korkolis, Y.P., Kinsey, B.L., Knezevic, M., 2020b. Experimental studies into the role of cyclic bending during stretching of dual-phase steel sheets. Int. J. Material Form. 13, 393–408.
Proust, G., Tomé, C., Kaschner, G., 2007. Modeling texture, twinning and hardening evolution during deformation of hexagonal materials. Acta Mater. 55, 2137–2148.
Qin, J., Zhou, C., Wang, D., Li, X., Hu, T., Wang, J., Yang, Y., 2023. Effects of microstructure and texture on the deep drawability of C10200 copper sheets. J. Mater. Res. Technol. 25, 773–785.
Ridha, A., Hutchinson, W., 1982. Recrystallisation mechanisms and the origin of cube texture in copper. Acta Metall. 30, 1929–1939.
Riyad, I.A., Clausen, B., Savage, D.J., Jeong, Y., Brown, D.W., Knezevic, M., 2024. Modeling deformation, recovery, and recrystallization of tantalum using a higher order elasto-viscoplastic self-consistent model. J. Mech. Phys. Solid. 194, 105925.
Riyad, I.A., Knezevic, M., 2023. Field fluctuations viscoplastic self-consistent crystal plasticity: applications to predicting texture evolution during deformation and recrystallization of cubic polycrystalline metals. Acta Mater. 261, 119395.
Roters, F., Eisenlohr, P., Hantcherli, L., Tjahjanto, D.D., Bieler, T.R., Raabe, D., 2010. Overview of constitutive laws, kinematics, homogenization and multiscale methods in crystal plasticity finite-element modeling: theory, experiments, applications. Acta Mater. 58, 1152–1211.
Segal, V., 2018. Review: modes and processes of severe plastic deformation (SPD). Materials 11.
Segurado, J., Lebensohn, R.A., Llorca, J., Tomé, C.N., 2012. Multiscale modeling of plasticity based on embedding the viscoplastic self-consistent formulation in implicit finite elements. Int. J. Plast. 28, 124–140.
Song, D., Ponte Castañeda, P., 2018. Fully optimized second-order homogenization estimates for the macroscopic response and texture evolution of low-symmetry viscoplastic polycrystals. Int. J. Plast. 110, 272–293.
Sun, Y., Zhou, K., Qiao, H., Xin, R., Wang, H., Wu, P., 2022. Crystal plasticity-based finite element modeling of twin transmission across grain boundaries in magnesium. Mater. Today Commun. 30, 102998.
Tam, K.J., Vaughan, M.W., Shen, L., Knezevic, M., Karaman, I., Proust, G., 2021. Modelling dynamic recrystallisation in magnesium alloy AZ31. Int. J. Plast. 142, 102995.
Tian, H., Brownell, B., Baral, M., Korkolis, Y.P., 2017. Earing in cup-drawing of anisotropic Al-6022-T4 sheets. Int. J. Material Form. 10, 329–343.
Toth, L.S., Estrin, Y., Lapovok, R., Gu, C.F., 2010. A model of grain fragmentation based on lattice curvature. Acta Mater. 58, 1782–1794.
Weiss, J., Knezevic, M., 2024. Effects of element type on accuracy of microstructural mesh crystal plasticity finite element simulations and comparisons with elasto-viscoplastic fast Fourier transform predictions. Comput. Mater. Sci. 240, 113002.
Wenk, H.R., Canova, G., Bréchet, Y., Flandin, L., 1997. A deformation-based model for recrystallization of anisotropic materials. Acta Mater. 45, 3283–3296.
Winther, G., Wright, J.P., Schmidt, S., Oddershede, J., 2017. Grain interaction mechanisms leading to intragranular orientation spread in tensile deformed bulk grains of interstitial-free steel. Int. J. Plast. 88, 108–125.
Yoon, S.C., Horita, Z., Kim, H.S., 2008. Finite element analysis of plastic deformation behavior during high pressure torsion processing. J. Mater. Process. Technol. 201, 32–36.
Zecevic, M., Beyerlein, I.J., Knezevic, M., 2018a. Activity of pyramidal I and II <c+a> slip in Mg alloys as revealed by texture development. J. Mech. Phys. Solid. 111, 290–307.
Zecevic, M., Beyerlein, I.J., McCabe, R.J., McWilliams, B.A., Knezevic, M., 2016a. Transitioning rate sensitivities across multiple length scales: microstructure-property relationships in the Taylor cylinder impact test on zirconium. Int. J. Plast. 84, 138–159.
Zecevic, M., Knezevic, M., 2015. A dislocation density based elasto-plastic self-consistent model for the prediction of cyclic deformation: application to Al6022-T4. Int. J. Plast. 72, 200–217.
Zecevic, M., Knezevic, M., 2018. A new visco-plastic self-consistent formulation implicit in dislocation-based hardening within implicit finite elements: application to high

strain rate and impact deformation of tantalum. Comput. Methods Appl. Mech. Eng. 341, 888–916.
Zecevic, M., Knezevic, M., 2019. An implicit formulation of the elasto-plastic self-consistent polycrystal plasticity model and its implementation in implicit finite elements. Mech. Mater. 136, 103065.
Zecevic, M., Knezevic, M., Beyerlein, I.J., McCabe, R.J., 2016b. Origin of texture development in orthorhombic uranium. Mater. Sci. Eng., A 665, 108–124.
Zecevic, M., Knezevic, M., McWilliams, B., Lebensohn, R.A., 2020. Modeling of the thermo-mechanical response and texture evolution of WE43 Mg alloy in the dynamic recrystallization regime using a viscoplastic self-consistent formulation. Int. J. Plast. 130, 102705.
Zecevic, M., Lebensohn, R.A., McCabe, R.J., Knezevic, M., 2018b. Modeling of intragranular misorientation and grain fragmentation in polycrystalline materials using the viscoplastic self-consistent formulation. Int. J. Plast. 109, 193–211.
Zecevic, M., Lebensohn, R.A., McCabe, R.J., Knezevic, M., 2019. Modelling recrystallization textures driven by intragranular fluctuations implemented in the viscoplastic self-consistent formulation. Acta Mater. 164, 530–546.
Zecevic, M., McCabe, R.J., Knezevic, M., 2015a. A new implementation of the spectral crystal plasticity framework in implicit finite elements. Mech. Mater. 84, 114–126.
Zecevic, M., McCabe, R.J., Knezevic, M., 2015b. A new implementation of the spectral crystal plasticity framework in implicit finite elements. Mech. Mater. 84, 114–126.
Zecevic, M., McCabe, R.J., Knezevic, M., 2015c. Spectral database solutions to elasto-viscoplasticity within finite elements: application to a cobalt-based FCC superalloy. Int. J. Plast. 70, 151–165.
Zecevic, M., Pantleon, W., Lebensohn, R.A., McCabe, R.J., Knezevic, M., 2017. Predicting intragranular misorientation distributions in polycrystalline metals using the viscoplastic self-consistent formulation. Acta Mater. 140, 398–410.
Zhang, J.X., Ma, M., Liu, W.C., 2017. Effect of initial grain size on the recrystallization and recrystallization texture of cold-rolled AA 5182 aluminum alloy. Mater. Sci. Eng., A 690, 233–243.
Zhilyaev, A.P., Langdon, T.G., 2008. Using high-pressure torsion for metal processing: fundamentals and applications. Prog. Mater. Sci. 53, 893–979.